Compact dual-wavelength depolarization lidar for aerosol characterization over the Subtropical North Atlantic

Yenny González[1,2], María F. Sánchez-Barrero[3], Ioana Popovici[1,3], África Barreto[2,4], Stephane Victori[1], Ellsworth J. Welton[5], Rosa D. García[6,2], Pablo G. Sicilia[2], Fernando A. Almansa[1,2], Carlos Torres[2], Philippe Goloub[3]

[1] Scientific department, CIMEL Electronique, Paris, 75011, France
[2] Izaña Atmospheric Research Centre (IARC), State Meteorological Agency (AEMET), Santa Cruz de Tenerife, 38001, Spain
[3] Univ. Lille, CNRS, UMR 8518 – LOA – Laboratoire d'Optique Atmosphérique, 59000 Lille, France
[4] Atmospheric Optics Group of Valladolid University (GOA–UVa), Valladolid University, Valladolid, 47002, Spain
[5] NASA Goddard Space Flight Center, Greenbelt, MD, 20771, USA.
[6] TRAGSATEC, Madrid, 28006, Spain.

Correspondence: Yenny González (y-gonzalez@cimel.fr)

Abstract. We present a comprehensive characterization of the optical properties of various aerosol types based on data collected using a compact dual-wavelength depolarization elastic lidar (532 and 808 nm, CIMEL CE376). This study evaluates the vertical distribution and temporal evolution of aerosols observed in the subtropical North Atlantic region, covering from Saharan dust, volcanic aerosols, and fresh and aged wildfire plumes. Measurements were conducted between August 2021 and August 2023, using a modified two-wavelength Klett inversion method to derive the aerosol backscatter and extinction coefficients from CE376 lidar measurements. To assess the performance of the CE376 system, an intercomparison campaign with an MPL-4B lidar (MPLNET) was conducted while both the systems were collocated at the Izaña Atmospheric Research Centre (Canary Islands, Spain). Both instruments depicted the vertical aerosol structure similarly. Discrepancies were primarily attributed to errors in determining the overlap function and depolarization calibration in each instrument, as well as the greater influence of solar background radiation on the CE376 system during daylight. Absolute differences in the volume depolarization ratio (δ^{v}) were 0.003, which decreased to 0.002 when only nighttime data were analyzed. The combination of the two channels of the CE376 provided valuable insights into particle linear depolarization (δ^{P}), extinction Ångström exponent (EAE (532/808)), and attenuated color ratio (ACR (808-532)). Fresh Saharan dust particles, characterized by large, non-spherical morphology and a well-mixed vertical layer, exhibited the lowest EAE (532/808), the highest ACR (808-532) and δ^{P} (532) > 0.15. In contrast, smaller particles with quasi homogeneous morphology were attributed to sulfate aerosols from the early stages of the Cumbre Vieja volcano eruption and aged Canadian wildfire plumes traveling across the Atlantic. These aerosols showed the lowest δ^{P} (0.03 for volcanic sulfate and 0.08 for aged wildfire aerosols) and the highest EAE (532/808) (1.5 and 1.2, respectively). Intermediate values of these retrieved parameters were associated to a heterogenous mixture of ash, soot, and charred vegetation from fresh local forest wildfires. The retrieved properties underscore the suitability of the CE376 micro-lidar for continuous monitoring and characterization of the temporal and vertical distribution of atmospheric aerosols.

1 Introduction

Atmospheric aerosols play a critical role in Earth's climate system; however, their effects on radiative forcing remain among the largest uncertainties in climate models (Boucher et al., 2013; Szopa et al., 2021, Forster et al., 2021). These uncertainties are primarily due to the heterogeneity of aerosol properties and their spatiotemporal variations. Consequently, continuous aerosol monitoring is essential. Ground-based remote sensing instruments, such as lidars and photometers, are well-suited for this purpose. Lidar systems provide detailed vertical profiles of aerosol characteristics, while photometers offer integrated

columnar information. The combination of these systems enables continuous monitoring of the temporal evolution and spatial distribution of aerosols, thereby reducing uncertainties in aerosol radiative impacts and improving understanding of their optical properties (Granados-Muñoz et al., 2014; Bovchaliuk et al., 2016; Tsekeri et al., 2017; Lopatin et al., 2021; Dos Santos Oliveira et al., 2023; López-Cayuela et al., 2023).

The extensive worldwide deployment of the CE318 sun-sky photometer through the open-access AERONET network (AErosol Robotic NETwork; Holben et al., 1998; Giles et al., 2019), has demonstrated its capability to provide multispectral and multiangular aerosol property data (Dubovik and King, 2000; Smirnov et al., 2000; Torres et al., 2017). Numerous studies have used photometer observations to reveal the heterogeneity of aerosol properties based on their sources and environmental conditions (Dubovik et al., 2002; Torres and Fuertes, 2021; Boichu et al., 2023). Lidar observations, although limited by the high cost and maintenance demands of the systems, contribute significantly to our knowledge of aerosol vertical variations. Advances in the use of ceilometers, originally designed for cloud base height detection using near-infrared light (Cazorla et al., 2017; Jin et al., 2018; Li et al., 2021; Adam et al., 2022; Bedoya-Velásquez et al., 2022), and micropulse lidar systems with low-power lasers (in the order of microjoules) in the visible spectrum (Welton et al., 2001; Campbell et al., 2002; Córdoba-Jabonero et al., 2021; Barreto et al., 2022a; López-Cayuela et al., 2022; Lopatin et al., 2024), have further enhanced aerosol monitoring. These systems provide valuable single-wavelength aerosol optical property data, especially when collocated with photometers (Mortier et al., 2013; Popovici et al., 2018, 2022; Bedoya-Velásquez et al., 2022; Lopatin et al., 2024). Moreover, the addition of polarization measurement capabilities has improved the differentiation of non-spherical particles, enabling enhanced aerosol typing (Burton et al., 2013; Groß et al., 2013; Floutsi et al., 2023; López-Cayuela et al., 2023).

As a solution for continuous monitoring of aerosol properties, the French company CIMEL proposes the combined use of the CE376 micropulse lidar (hereafter CE376), featuring two wavelengths and polarization capabilities, alongside the CE318-T sun-sky-lunar photometer (Barreto et al., 2016). The addition of a second wavelength to the lidar enables insights into aerosol size distributions. Previous studies using the CE376 have highlighted its atmospheric monitoring capabilities (Riandet et al., 2023; Papetta et al., 2024). The combined use of the CE376 and CE318-T was first presented by Sanchez-Barrero et al. (2024).

This study was conducted at the Izaña Atmospheric Research Centre (IARC, 28.31° N, 16.50° W), a multiplatform site providing long-term measurements of atmospheric chemical and aerosol species (Cuevas et al., 2024), operated by the State Meteorological Agency of Spain (AEMET). The observatory is also part of ACTRIS (Aerosol, Clouds and Trace Gases Research Infrastructure) European Research Infrastructure (Laj et al., 2024) as a Central Facility for aerosol remote sensing. Located at 2,367 meters above sea level (average pressure of 770 hPa), in the vicinity of Teide National Park (Canary Islands), the site benefits from stable atmospheric conditions largely governed by the quasi-permanent northwest subsidence regime of the Hadley cell, and well-stratified lower troposphere, with strong temperature inversion layer often situated between 900 and 800 hPa (Cuevas, 1995; Carrillo et al., 2016). Background conditions prevail for most of the year, occurring more frequently between April and June. In contrast, dust-loaded Saharan air masses dominate in July and August (Barreto et al.,2022b). These alternating conditions make Izaña an ideal location for studying regional aerosol transport in the subtropical North Atlantic.

The motivation for this paper is twofold. First, we introduced an uninterrupted 18-day intercomparison campaign to evaluate the performance of a CE376 relative to the MPL-4B lidar operated by the NASA Micro Pulse Lidar Network (MPLNET) (Welton et al., 2001, Welton et al., 2018), with both systems collocated at Izaña. Second, we provide a comprehensive aerosol characterization based on optical properties derived from CE376 profiles, focusing on Saharan dust outbreaks, volcanic eruptions and wildfire aerosols observed between August 2021 and August 2023.

Section 2 outlines the instrumentation and methodology used to derive columnar aerosol properties. Section 3 presents the results, with Sect. 3.1 detailing the intercomparison campaign, and Sect. 3.2 exploring aerosol properties under different scenarios: Saharan dust (Sect. 3.2.1), volcanic aerosols (Sect. 3.2.2) and wildfire aerosols (Sect. 3.2.3). Sect. 3.3 summarizes the observations, providing an aerosol classification. The main conclusions of this study are summarized in Sect. 4.

2 Instrumentation and methodology

2.1 The CE376 lidar

The CE376 is an autonomous, compact, and lightweight eye-safe lidar system designed to measure elastic backscattered light and depolarization at two wavelengths: 532 nm and 808 nm. It utilizes a pulsed Nd:YAG laser at 532 nm with an energy of 5.8 μJ, a pulse width of 0.89 ns, and a pulse repetition rate of 4.6 kHz. The laser beam is directed through a set of dichroic mirrors and collimation lenses. The half-angle field of view (FOV) for the 532 nm channel is 50 μrad for emission and 120 μrad for reception. For the 808 nm channel, the system employs a pulsed laser diode with a narrow spectral linewidth of 0.6 nm, achieved through a volume Bragg grating (VBG). This laser operates with an energy of 1.9 μJ and a repetition rate of 4.7 kHz. The laser diode is coupled to an optical fibre and collimation lenses. The half-angle FOV for the 808 nm channel is broader, with emission half-angle FOV of 225 μrad and a reception of 255 μrad. The optical design of the CE376 consists of two Galilean telescopes in a biaxial configuration. The elastic backscattered light at each wavelength is collected and detected using Excelitas avalanche photodiode detectors operating in single-photon counting mode (SPCM-APD) at rates of up to 40 MHz. These detectors have a dead time ranging from 23 to 28 ns. The electronic control and data acquisition cards were developed by CIMEL. They also include a Field-Programmable Gate Array (FPGA) for multichannel sequencing and counting implemented with internally developed Hardware Description Language (HDL) code, and a microcontroller-based board for laser power, temperature, and security control and monitoring. Additionally, it features a fully digital power and timing control system, as well as a USB-based communication interface.

The system features a range resolution of 15 meters and operates continuously (24/7), with 1-minute integration intervals. Linear depolarization is measured at both the 532 nm and 808 nm channels, significantly enhancing its aerosol characterization capabilities. Depolarization measurements are achieved by splitting the backscattered light into parallel and perpendicular components relative to the incident plane using Polarizing Beamsplitter Cubes (PBS). In this model, the polarization plane of the incident light is regulated with an accuracy of 2 degrees with manual Half-Wave Plates (HWP) positioned in front of the PBS within each channel. Unlike high-power lidars, which often require specialized laboratories, frequent maintenance interventions, and are more susceptible to adverse meteorological conditions, the CE376 is versatile and easier to deploy in field settings.

2.1.1 Signal processing and calibrations

The backscattered light from molecules and aerosols at a distance r in the atmosphere is detected at two wavelengths, 532 and 808 nm, in two configurations: parallel (||) and perpendicular (X) polarized signals to the receiver (532 ||, 532 X, 808 || and 808 X). The detected elastic backscattered signal, known as the range-corrected signal (RCS, in Ph s^{-1} m^2), undergoes a series of instrumental corrections for the SPCM detector linearity, background, overlap function O(r), and range dependence (r^2) at each channel. The RCS equation (Eq. 1; Weitkamp, 2005) includes information about: 1) the calibration constant $C_{L,\lambda}$ expressed in [Ph s^{-1} m^3 sr], which depends on the lidar system, 2) the backscatter coefficient, β(r), that represents the light scattered back to the system, in [$m^{-1}sr^{-1}$]; and 3) the atmospheric transmission losses due to the scattering and absorption of light by aerosols and molecules, T^2. The contributions of aerosols and molecules are expressed with the subscripts a and m, respectively. Therefore α(r) is the extinction coefficient in [m^{-1}] (Eq. 2):

$$RCS(\lambda, r) = C_{L,\lambda}[\beta_m(\lambda, r)+\beta_a(\lambda, r)]T^2_{mol}(\lambda, r)T^2_a(\lambda, r), \quad (1)$$

$$T^2_{mol}(\lambda, r)T^2_a(\lambda, r) = \exp\left(-2\int_0^r \alpha_{mol}(\lambda, r')dr'\right) \exp\left(-2\int_0^r \alpha_a(\lambda, r')dr'\right) \quad (2)$$

The second integral term in Eq. 2 is known as aerosol optical depth (AOD). Notice that the total atmospheric column AOD measured by the photometer is used as a reference (AOD_{Ph}). Using the Ångström law and with the information of AOD of the photometer (AOD_{Ph}) at 440 nm and extinction Ånsgtröm exponent calculated with the 440 and 880 nm channels of the photometer (EAE_{Ph} (440/880)), we obtain the AOD_{Ph} at 532 nm and 808 nm. The total signal RCS at each wavelength is defined by summing the parallel and perpendicular components and applying the relative amplification factor V* according to the polarization calibration (Freudenthaler et al., 2009).

We follow the standard procedure of the European Aerosol Research Lidar Network (EARLINET) (Pappalardo et al., 2014) of performing a Rayleigh fit to check the far-range accuracy and the laser pointing alignment of the CE376. The procedure consists of normalizing the RCS (λ, r) to the attenuated molecular backscatter coefficient ($\beta_{mol\text{-}att}$ (λ, r) = β_{mol} (λ, r)·T_{mol}^2 (λ, r)) in a range free of aerosols (r_{ref}). The molecular properties (β_{mol} (λ, r) and T_{mol}^2 (λ, r)) can be determined from pressure and temperature profiles from radiosondes or as approximations from standard atmospheric models. The same procedure can be used to determine $C_{L,\lambda}$, where the unknown term, T_a^2 (λ, r_{ref}), can be obtained from a collocated sun-moon photometer when it is available (Cazorla et al., 2017). The total attenuated backscatter coefficient, β_{att} (λ, r), is defined as the ratio between the RCS and the lidar constant (Eq. 3), which describes purely atmospheric parameters.

$$\beta_{att}(\lambda, r) = RCS(\lambda, r)/C_{L,\lambda} = [\beta_{mol}(\lambda, r) + \beta_a(\lambda, r)]T_{mol}^2(\lambda, r)T_a^2(\lambda, r) \quad (3)$$

In addition, the volume linear depolarization ratio (δ^v) and the attenuated colour ratio (ACR) are directly derived from the CE376 observations. Both δ^v and ACR account for molecular and aerosol contributions, however, they can be considered as a first approximation of the aerosol properties, providing valuable information on the particle morphology.

δ^v is defined as the ratio of cross-polarized to co-polarized backscattered light from the atmosphere and derived following the methods of Freudenthaler et al. (2009). The polarization channels are calibrated using the Δ90° method (Freudenthaler, 2016) method, leading to less than 5% uncertainty on V* for δ^v values up to 0.3. Calibration coefficients determined in July 2021 were used for data from August 2021 to October 2022. Wire grid polarizers were added to the PBS cubes to reduce crosstalk in November 2022. New calibration coefficients were determined and used to evaluate the data set collected between November 2022 and August 2023.

The ACR (Eq. 4) approximates to the color ratio (CR) and provides insights into particle size (Omar et al., 2009; Burton et al., 2013; Wang et al., 2020; Qi et al., 2021). The β_{att} (λ,r) corrected by the two-way molecular transmittance T_{mol}^2 (λ, r) is given as a first calculation to the aerosol backscatter, as done by the CALIPSO (Cloud-Aerosol Lidar and Infrared Pathfinder Satellite Observation) algorithms (Omar et al., 2009). Under the assumption that a single aerosol type is homogeneously distributed in the atmosphere, the ACR with values between 0 and 1 indicates presence of fine to large particles, respectively.

$$ACR(r) = \frac{\beta_{att}(808,r)\, T_{mol}^{-2}(808,r)}{\beta_{att}(532,r)\, T_{mol}^{-2}(532,r)} = \frac{[\beta_{mol}(808,r)+\beta_a(808,r)]}{[\beta_{mol}(532,r)+\beta_a(532,r)]} \exp(-2\int_0^r [\alpha_a(808,r') - \alpha_a(532,r')]dr') \quad (4)$$

2.1.2 Derived aerosol properties

A modified two-wavelength Klett inversion is used to derive the aerosol backscatter and extinction coefficients from the CE376 observations (Sanchez-Barrero et al., 2024). The inversion scheme includes the well-known Klett solution (Klett, 1985; Weitkamp, 2005) in either of its integration forms, specified by the position of the boundary conditions. The backward (far end at an aerosol-free region r_{ref}) and forward (near end, close to the ground r_0) Klett solutions are applied according to the range detection limits at each wavelength, assuming a constant extinction-to-backscatter ratio (i.e., lidar ratio LR). This contrasts with high-power Raman or HSRL (High Spectral Resolution Lidar) lidar systems, which can retrieve vertically resolved LR profiles independent of photometer information, providing higher vertical resolution and accuracy in some applications, especially during nighttime (Weitkamp, 2005; Ansman et al., 1990; Shipley et al., 1983). The detection limits of the CE376 are determined by the signal-to-noise ratio (SNR). In this work, detection limits are calculated using SNR =1.5. We effectively retrieved the LR by iteration until the AOD derived from the solution converges to the measured value by the collocated CE318-T photometer. During nighttime, the Klett backward solution is applicable for both, 532 and 808 nm wavelengths due to higher detection limits. During daytime operations, the 808 nm channel is more susceptible to solar background noise due to their larger FOV, and the lower pulse energy of the emitted laser beam compared to the 532 nm channel. The increased FOV leads to a greater collection of ambient solar radiation, and when combined with the lower pulse energy, reduces the signal-to-noise ratio. This limitation lowers the detection capability of the 808 nm channel to below 2 km above ground level. To address this, the forward solution is employed, and the inversion constrained using an estimated AOD for the reduced profile at 808 nm (Sanchez-Barrero et al., 2024). In contrast, the 532 nm channel benefits from a narrower FOV and higher pulse energy, making it less affected by solar background under similar conditions. This allows the 532 nm

channel to achieve a higher detection limit compared to the 808 nm channel. Consequently, the effect of solar background noise on the 532 nm channel is less severe and typically occurs at higher altitudes, where the retrieval process is less affected.

As a result of the inversion, we obtain profiles of aerosol backscatter and extinction at the two wavelengths. Additional parameters are the color ratio (CR) from the pair of backscatter profiles ($\beta_a(\lambda, r)$), and the $EAE_{lid}(532/808, r)$. Both parameters provide insights into aerosol size. Furthermore, by combining the depolarization observations with the retrieved backscatter coefficients, we derive the particle linear depolarization ratio (δ^p), defined by Eq. 5. The molecular depolarization ratio (δ^{mol}) is the theoretical value according to the bandwidth of the filter in front the half-wave plate in a CE376 system (δ^{mol} ~0.004) and R is the backscatter ratio, R= $(\beta_a(r) + \beta_{mol}(r))/\beta_{mol}(r)$. δ^P gives insights on the aerosol shape with low values (close to 0) indicating spherical aerosols and values above 0.2 indicating predominance of non-spherical aerosols (Gasteiger and Freudenthaler, 2014; Floutsi et al., 2023).

$$\delta^p(r) = \frac{[1+\delta^{mol}]\,\delta^v(r)R(r) - [1+\delta^v(r)]\,\delta^{mol}}{[1+\delta^{mol}]R(r) - [1+\delta^v(r)]} \quad (5)$$

Detailed procedures and uncertainties are addressed in Sanchez-Barrero et al. (2024). The overlap function and polarization calibration coefficients were determined using the data analysis software developed by CIMEL Electronique, called iAAMS. Additional software developments used in this study were performed in the frame of the joint laboratory between CIMEL and the LOA (Laboratoire d'Optique Atmosphérique) called AGORA-Lab.

The CE376 system at Izaña effectively achieves full overlap at altitudes of 2.6 km above ground level (a.g.l.) for the 532 nm channel and at 1.9 km a.g.l. for the 808 nm channel. Below these reference points, the optical efficiency is enhanced by correcting the lidar signal using the overlap function. During the study period, the instrument underwent optical alignment and depolarization calibration twice – in July 2021 and November 2022. For each period, an overlap function was determined using at least 3 profiles measured over 4 h on different aerosol-free nights (AOD< 0.03 at 500 nm). The uncertainty associated with these overlap functions, expressed as the standard deviation from the mean, ranges from 4% in the parallel 532 nm channel up to 10% in the 808 nm channel in the first kilometer of altitude. These uncertainties in the overlap function are in the magnitude of 10% proposed by Welton and Campbell (2002). Data below 400 m a.g.l. are excluded from consideration due to increased uncertainties resulting from detector saturation at close range.

2.2 The CE318-T photometer

The CE376 uses the AOD data from the collocated CE318-T master photometer at Izaña station to better constrain the Klett-Fernald solution. This photometer manufactured by CIMEL, performs direct solar and lunar irradiance measurements at nine wavelengths (340, 380, 440, 500, 670, 870, 936, 1020, and 1640 nm; Barreto et al., 2016). The instrument derives spectral AOD with an accuracy up to 0.01, with higher uncertainties in the UV channels. The extinction Ånsgtröm exponent (EAE) is determined by pairs of AOD values at different wavelengths and provides information of the aerosol size (Ångström 1929; Kusmierczyk-Michulec, 2002). Automatic near real time aerosols properties are retrieved by the CE318-T at Izaña following the AERONET standards (AERONET; https://aeronet.gsfc.nasa.gov) (Holben et al, 1998; Giles et al, 2019). Aerosols microphysical properties, such as volume size distribution (VSD), refractive index and single-scattering albedo can also be retrieved from multi-angular sky radiance measurements and inversion procedures (Dubovik and King, 2000; Sinyuk et al, 2020).

2.3 The MPL-4B lidar

The MPL-4B operates at 532 nm with depolarization capability in a 24/7 mode. It is characterized with a low pulse energy (5-6 μJ) laser with a repetition rate of 2.5 kHz and depolarization detection (Campbell et al., 2002; Flynn et al., 2007; Welton et al., 2018). Unlike the CE376, the MPL-4B has a monoaxial configuration which results in a long overlap range (typically beyond 3 km) but does simplify some aspects of the polarization calibration. MPLNET manages the MPL-4B calibrations, signal processing, and retrieval products. The primary calibrations include detector deadtime and dark current, laser-detector cross-talk (afterpulse), overlap, and polarization (Campbell et al., 2002, Welton et al., 2018). Relative attenuated backscatter

signals and uncertainties are processed (Welton and Campbell, 2002), and the resulting data are used to retrieve a wide variety of variables in their product suite, with error propagation methods producing uncertainties for the retrieved variables. MPLNET Version 3, Level 1.5 signal data and aerosol product (Welton et al., 2000; Welton et al., 2002) were used in this study.

3 Results and discussion

3.1 Intercomparison between the CE376 and MPL-4B

We conducted an intercomparison of the aerosol products from the CE376 and MPL-4B micro-pulse lidars. The CE376 was installed in August 2021 at Izaña, while the MPL-4B has been measuring at the site since February 2020. The instruments were in separate buildings distancing 223 meters, within the facilities of the Izaña observatory (Fig. 1). Considering the extensive usage and established reputation of the MPLNET data, along with the MPL-4B design similarities to the CE376, we view this intercomparison campaign as an ideal opportunity to demonstrate the capabilities of the CE376. However, in this study we emphasize that the MPL-4B used here relates to the MPLNET deployed and managed instrument type, not those operated outside MPLNET as calibration and processing methods may be different.

As explained in Sanchez-Barrero et al. (2024), the uncertainties associated to each retrieved parameter in the CE376 system is calculated using error propagation based on first-order derivatives, as described in the literature referenced therein. In the CE376 model, the main sources of error are the estimation of the overlap function, background noise, lidar constant, and depolarization calibrations. Our uncertainties in the overlap function varied from 4% in the parallel 532 nm channel up to 10% in the 808 nm channel within the first kilometer of altitude, and those in the depolarization calibration were estimated to less than 5%. In addition, relative errors > 15% in the extinction coefficients lead to absolute uncertainties > 0.5 in EAE (Sanchez-Barrero et al. 2024 and references therein). Both instruments use the AOD data (with 0.01 uncertainty) from the AERONET photometer collocated at Izaña (hereafter AOD_{Ph}), to better constrain the Klett-Fernald solution when available. The uncertainty in the retrieved LR is estimated by the convergence within the AOD uncertainties (0.01) in the iterative Klett solution (Sect. 3.2 in Sanchez-Barrero et al., 2024). To compare the aerosol products of both systems, the CE376 profiles collected with a vertical resolution of 15 m were averaged to the 75 m vertical resolution of the MPL.

We used the first period of collocated measurements to conduct an intercomparison campaign. For a span of 18 days (August 13–30, 2021), both the CE376 and the MPL-4B were engaged in measurements at the Izaña site. We analyzed the volume and particle linear depolarization ratios (δ^v and δ^p), attenuated backscatter (β_{att}) and extinction (α_a) coefficient profiles measured at 532 nm with both, the MPL-4B (version 3 products) and the CE376. An overview of the atmospheric aerosol properties observed by the CE376 during the campaign period is shown in Fig. 1a–e. Measurements of β_{att} at 808 nm, α_a at 532 nm, δ^v at 532 nm, ACR (808-532) recorded with the CE376, as well as AOD and EAE_{Ph} (532/808) from the collocated photometer at Izaña Observatory, describe the temporal and vertical evolution of the aerosol dust event. The spatial extent of the Saharan dust layer(s) over the Canary Islands on August 16, 2021, can be observed in the MODIS VIS channel satellite image shown in Fig. 1g.

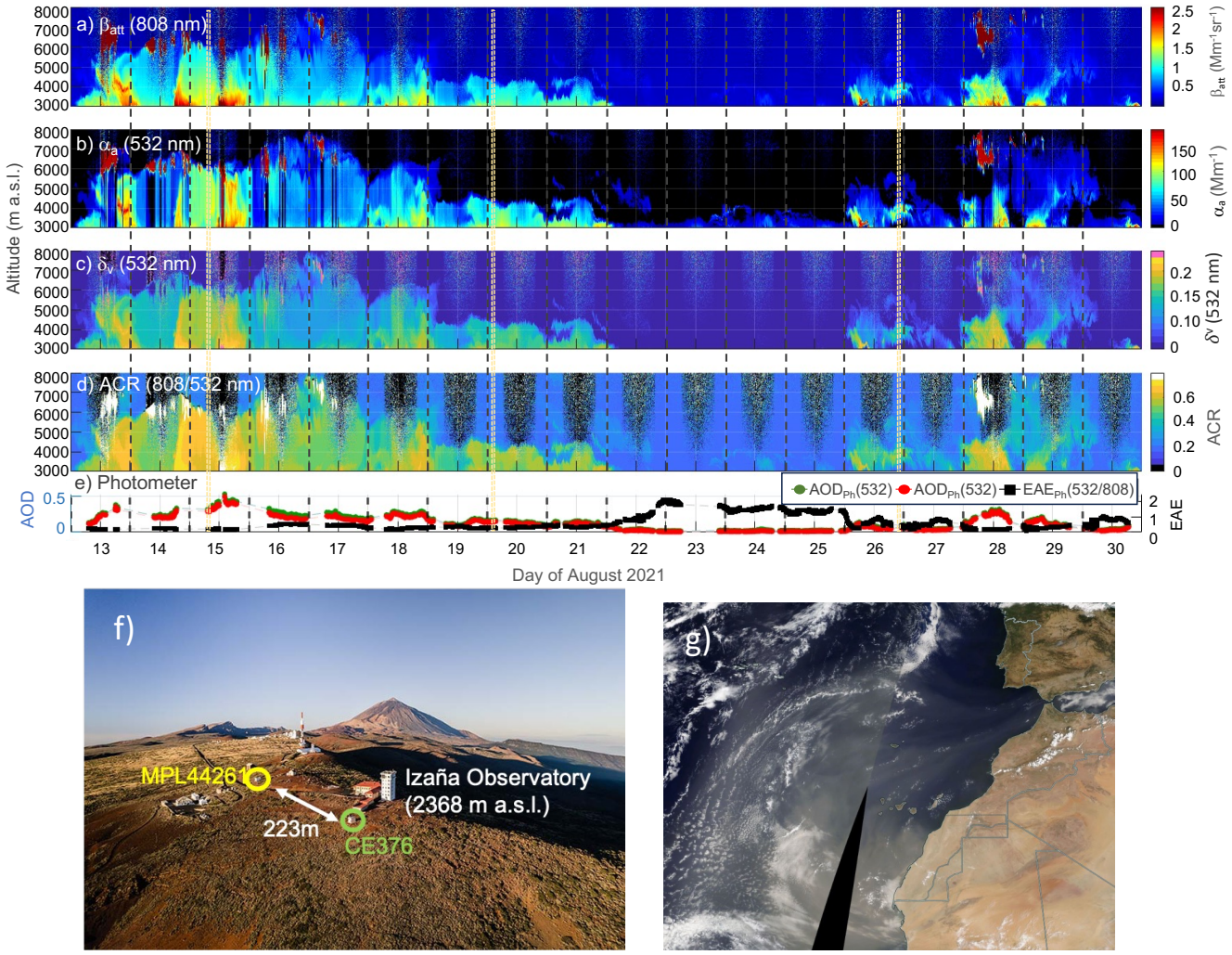

Figure 1. Measurements of a) attenuated backscatter (β_{att}) at 808 nm, b) aerosol extinction (α_a) at 532 nm, c) volume linear depolarization ratio (δ^v) at 532 nm, d) attenuated color ratio (ACR) from the CE376, along with e) AOD at 532 and 808 nm (AOD_{Ph} (532) and AOD_{Ph} (808)) and extinction Ångström exponent (EAE_{Ph} (532/808)) from the collocated photometer during the intercomparison period with the MPL4B. The aerosol properties registered during this period describe the influence of the Saharan Air Layer over Izaña during summer. Yellow dashed bars in (a)-(e) highlight the time frames selected to calculate the averaged profiles described in Fig. 2. f) Location of the CE376 and MPL44161 lidar systems at Montaña de Izaña during the comparison campaign carried out in August 2021. Photo courtesy of Pekka Pelkonen (The Integrated Carbon Observation System, ICOS RI). g) MODIS VIS channel satellite image showing the Saharan dust over the Canary Islands on August 16, 2021 (https://firms.modaps.eosdis.nasa.gov, [accessed on June 16, 2024]).

From August 14–18, 2021, a relatively homogeneous layer of Saharan dust aerosols from North Africa of nearly 7 km of thickness arrived to Izaña. During this period, δ^v reached values close to 0.2, AOD ~ 0.3 at 532 nm and EAE_{Ph} (532/808) of 0.2–0.5 in agreement with previous studies (Fig. 1c, Freudenthaler et al., 2009; Haarig et al., 2022). In the following days, August 19–21, 2021, the dust layer gradually diminished (3.5 km of thickness, EAE_{Ph} (532/808) ~ 0.3) and then lead to the characteristic maritime clean aerosol conditions at the site (August 23–25, 2021, Fig. 1c). Subsequently, on August 25–26, 2021, air masses from southern regions of the African continent (South of Mauritania, Senegal and Niger) were detected at

Izaña evolving from fine, low depolarizing particles (δ^v = 0.03±0.01, EAE_{Ph} (532/808) ~ 0.4, Fig. 1c) to coarser and higher depolarizing particles by August 28, 2021 (δ^v ~0.2 and EAE_{Ph} (532/808) ~0.3, Fig. 1c). The temporal evolution and intensity of the Saharan dust event is also well described using the combined information given by the parameters δ^v (532), α_a (532) and ACR (808-532). The highest values accurately depict the peak of the dust episode, followed by a decline as the dust dissipates.

To estimate the overall difference between the CE376 and the MPL4B, we calculated the 15-min averaged δ^v (532) profiles measured simultaneously by the two instruments over the entire study period. The retrievals of the CE376 were defined with a blind zone of 400 m at 532 nm and 350 m at 808 nm, based on the overlap function. Using the whole data set, the absolute difference in the retrieved LR (532) is 9±14 sr, that drops to 2±13 sr when night-time data (21:00–06:00 UTC) is used. The absolute differences between the CE376 and the MPL4B on δ^v (532) using 15-min average signals, were 0.003±0.005 (mean±std) in the first 4 km of the profiles (6.5 km a.s.l) using the full-day dataset. Above this altitude, the difference between the two instruments increases during daylight, mainly due to the larger effect of the solar background on the CE376 (0.01±0.06). This effect is particularly pronounced during the summer months at the site's latitudes when the sun is near the zenith. The absolute differences in δ^v decrease to 0.002±0.01 along the 7.5 km of the profile (10 km a.s.l.) when only the data collected during nighttime is selected. The absolute differences on α_a and β_a, both derived at 532 nm by the two instruments, were 1.3±3.2 Mm^{-1} and 0.14±0.12 $Mm^{-1}sr^{-1}$, respectively. This absolute difference was calculated as the difference between the 15-min average signals and using the first 4 km of the profile (6.5 km a.s.l) and the complete dataset. The absolute differences in extinction and backscatter were also reduced when only nighttime data is used.

In Fig. 2, we selected three different time frames (T1, T2, T3) that summarize the significant variability of dust aerosol profiles during the comparison. The aerosol properties presented in Fig. 2 (from left to right) are δ^v (532, 808), α_a (532, 808), β_a (532, 808), δ^p (532, 808), EAE (532/808) from the CE376 and the collocated photometer, and CR (808-532) and ACR (808-532). Each row represents a specific time frame based on 15-minute averages. Profiles of δ^v, δ^p, β_a and α_a, acquired simultaneously by the CE376 (in green dots) and MPL-4B at 532 nm (blue lines), highlight the good agreement between the two instruments, depicting the vertical aerosol structure similarly. Minor discrepancies in magnitude are mainly attributed to errors arising from the determination of the overlap function and the depolarization calibration in each instrument.

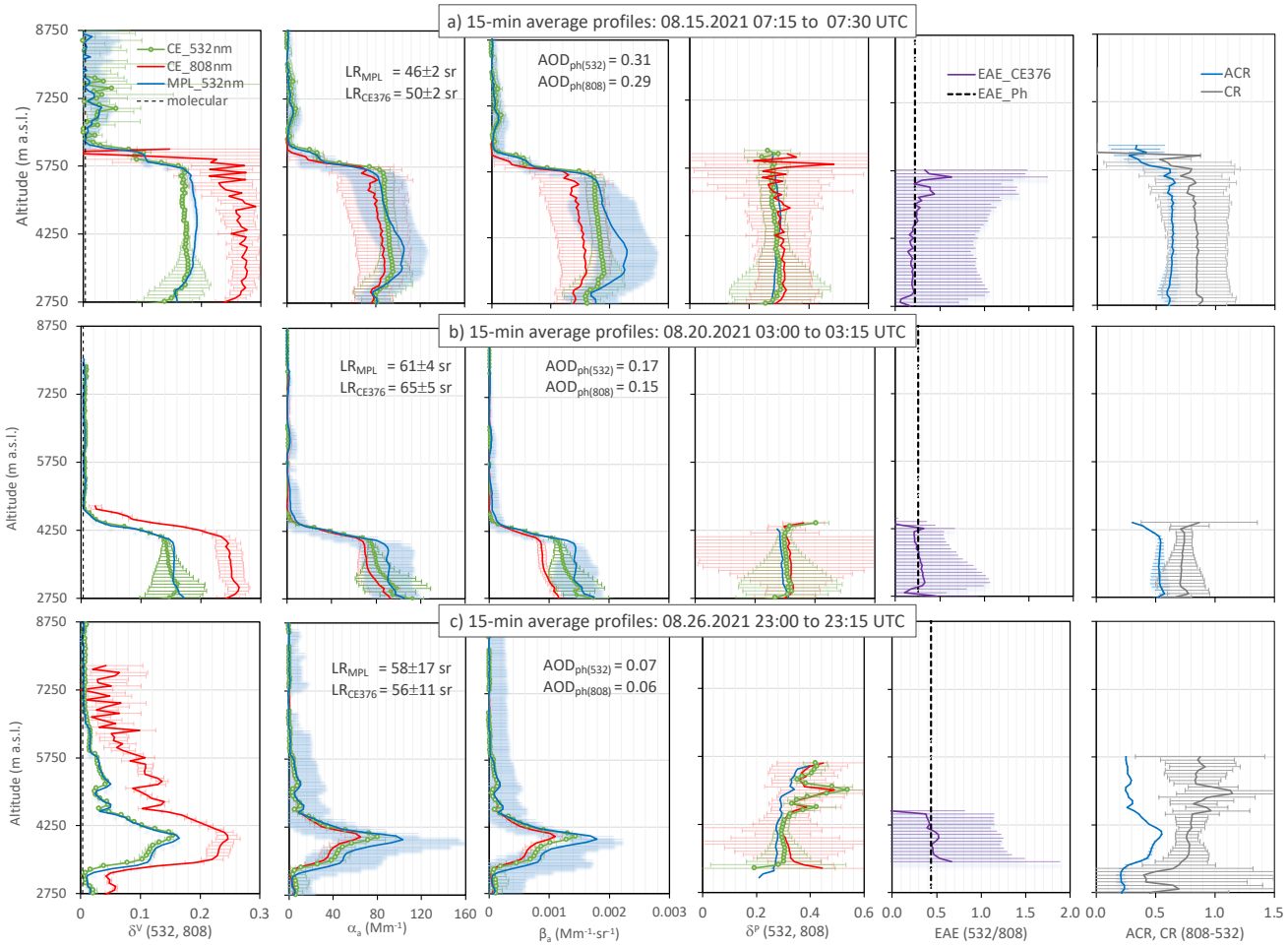

Figure 2. Three examples showing dust aerosol profiles depicting the Saharan Air Layer in August 2021. Each row represents a 15-min profile on a particular time of a selected day and each column the different retrieved parameters. Each example includes profiles of δ^v, α_a, β_a and particle linear depolarization (δ^p), acquired simultaneously by the CE376 (green dots) and MPL-4B (blue lines) at 532 nm. The profiles measured simultaneously at 808 nm by the CE376 (red lines) are also included. Profiles of extinction Ångstrom exponent (EAE_{Lid} (532/808)), color ratio (CR (808-532)) and attenuated color ratio (ACR (808-532)) determined with the CE376 are also shown. The EAE from the collocated photometer (EAE_{Ph} (532/808)) is also included. These examples are highlighted as yellow dashed bars in Fig. 1a–e.

3.2 Distribution of aerosol properties derived from CE376

Continuous monitoring of aerosol vertical profiles offers valuable information about the vertical distribution, temporal evolution, size, and composition of various aerosol types observed at a site. In this section, we present a detailed description of several vertical profiles recorded by the CE376 during four distinct aerosol events and we explore the insights provided using two wavelengths of the CE376 for aerosol characterization.

3.2.1 Saharan dust aerosols

We used the data collected in August 2021, as presented in the previous section, to further analyze the aerosol properties of Saharan dust particles observed at Izaña during summer. An extensive characterization of the climatology and aerosol properties of the summer Saharan Air Layer (SAL) has been already carried out in previous studies at the site using in-situ and remote sensing instrumentation (Rodríguez et al., 2011; Barreto et al. 2022a). The export of Saharan dust towards the Atlantic Ocean during summertime critically depends on the interannual variability of the large-scale meteorology over Northwestern Africa (Rodríguez et al., 2015). The summer SAL is a quite well-mixed dry dust aerosol layer that usually extends to 6 km height. At Izaña, this layer typically shows a maximum peak around 2.5 km a.s.l. with aerosol extinction coefficients (α_a (532)) > 65 Mm^{-1} (Barreto et al., 2022a). While the particles transported within the summer SAL are primarily soil dust emissions, traces of particulate pollutants—mainly associated with oil refineries, the fertilizer industry, and power plants in Northern and Eastern Algeria, Tunisia, and along the Atlantic coast of Morocco—have also been detected (Mereuţă et al., 2022; Rodríguez et al., 2011). Due to the proximity of the measurement site to the African coast, we consider these emissions to be fresh Saharan dust emissions.

Variations on the temporal and vertical evolution of aerosol properties of the dust event from August 2021 is summarized in Fig. 2:

(a) T1 (2021-08-15 07:15 to 07:30 UTC, Fig. 2a): This profile represents the dust event observed at Izaña from August 14–18, 2021. The event was characterized by a highly depolarizing layer of non-spherical aerosols (δ^v (532) ~0.17, δ^p (532) ~0.29) reaching an altitude of 6.2 km a.s.l. The aerosol load of the layer was relatively high, with an AOD of 0.32 at 532 nm and 0.28 at 808 nm. The retrieved LR was 50±2 sr at 532 nm and 55±1 sr at 808 nm, respectively. The layer also exhibited relatively high aerosol extinction (α_a (532) ~90 Mm^{-1} and α_a (808) ~80 Mm^{-1}) and backscatter coefficients (β_a (532) ~1.9 $Mm^{-1}sr^{-1}$ and β_a (808) ~1.6 $Mm^{-1}sr^{-1}$). The derived EAE_{Lid} (532/808) matched that from the photometer (EAE_{Ph} (532/808) = 0.22) throughout the entire layer, highlighting its homogeneity along the whole column. Additionally, ACR values of ~0.6 along the layer emphasized the presence of coarse aerosols along the well-mixed layer.

(b) T2 (2021-08-20 03:00 to 03:15 UTC, Fig. 2b): This profile represents the dust event observed at Izaña from August 19-21, 2021. A lower layer of dust particles (~4.3 km a.s.l.) presented similar properties to those observed in the previous days. The profile showed slightly lower depolarization (δ^v (532) ~0.15), aerosol load (AOD (532) = 0.17 and AOD (808) =0.15), aerosol extinction (α_a (532) ~80 Mm^{-1} and α_a (808) ~70 Mm^{-1}), aerosol backscatter (β_a (532) ~1.2 $Mm^{-1}sr^{-1}$, β_a (808) ~0.9 $Mm^{-1}sr^{-1}$) and ACR (808-532, ~0.5); but similar δ^p. The retrieved LR was higher than in the previous event, with values of 61±4 sr at 532 nm and 65±5 sr at 808 nm. The derived EAE_{Lid}, in line with that from the photometer (EAE_{Ph} (532/808) = 0.26), once again highlights the homogeneity of the aerosol properties within the layer.

(c) T3 (2021-08-26 23:00 to 23:15 UTC, Fig. 2c): This profile represents the arrival of a new dust layer at the site, featuring a layer between 3.5 and 4.5 km a.s.l. with a peak in aerosol properties around 4 km a.s.l. This episode originated at the same latitudes as the previous event. At its peak, the aerosol properties were similar to those observed in the previous dust episode: δ^v (532) ~0.16, δ^v (808) ~0.25, δ^p (532, 808) ~0.3, α_a (532) ~80 Mm^{-1}, and α_a (808) ~65 Mm^{-1}, β_a (532) ~1.4 $Mm^{-1}sr^{-1}$ and β_a (808) ~1.1 $Mm^{-1}sr^{-1}$. Both, EAE_{Lid} and the EAE_{Ph} (532/808), were approximately 0.43. An ACR (808-532) of ~0.5–0.6 was observed. The aerosol load along the column was relatively low (0.07 and 0.06 at 532 and 808 nm), resulting in high errors in the lidar ratios (58±17 sr at 532 nm and 56±16 sr at 808 nm). During the 18-days of Saharan dust intrusions studied here, we generally observe a larger depolarization effect with longer wavelengths due to the non-sphericity of large Saharan dust aerosols.

3.2.2 Volcanic aerosols

The eruptive period of the Cumbre Vieja Volcano lasted 85 days (La Palma, Canary Islands, Spain; Fig. 3f), from September 19 to December 13, 2021. Continuous monitoring of the eruption was made possible by the collaborative efforts of scientific, private, and governmental organizations. At the beginning of the eruption, fresh volcanic emissions, including sulfuric emissions, were measured on the islands. Approximately 1.8 Tg of sulfur dioxide (SO_2) was injected into the troposphere at altitudes between 3 and up to 6 km (Bedoya-Velásquez et al., 2022; Milford et al., 2023). The Tropospheric Monitoring

Instrument (TROPOMI) satellite onboard the Copernicus Sentinel-5 Precursor (S-5P) satellite measured volcanic SO_2 total column densities up to 20 Dobson Units (DU) (Fig. 3h, 2024). The S-5P, which has been orbiting in a sun synchronous polar orbit with an equator crossing at 13:30 local solar time since August 2019, offers high spectral covering from ultraviolet to shortwave infrared wavelengths and a spatial resolution of 5.5×3.5 km^2 (Theis et al., 2017). At the Izaña Observatory, located 140 km from the volcano (Fig. 3g), SO_2 concentrations up to 7700 μg m^{-3} were measured (Milford et al., 2023). Subsequent changes in atmospheric conditions led to the mixing of volcanic aerosols and desert dust in the region.

Figure 3a–e shows an overview of the atmospheric aerosol properties observed during September 23–24, 2021. Temporal evolution of β_{att} (808), α_a (532), δ^v (532), ACR (808-532) from the CE376, along with AOD and EAE from the collocated photometer over these two days, highlighting the presence of sulfuric plumes from the Cumbre Vieja volcano over the Izaña Observatory. A thin aerosol plume around 4 km a.s.l. was observed on September 23, 2021, followed by a thicker aerosol layer descending from 6 to 4 km a.sl. in the following day (Fig. 3a–d). These layers show relative high concentrations (β_a (808): 0.5–0.8 Mm^{-1}sr^{-1}, α_a (532): 40–100 Mm^{-1}, and AOD_{Ph} (532): 0.05–0.15) of nearly non-depolarizing (δ^v (532) < 0.05) fine aerosols (EAE_{Ph} (532/808): 1.5–2.0 and ACR <0.4). Similarly, VSD from AERONET show higher concentration of aerosols in the fine mode (radius of 0.15 μm) over the coarse mode (data available in the AERONET website, not shown for the sake of brevity).

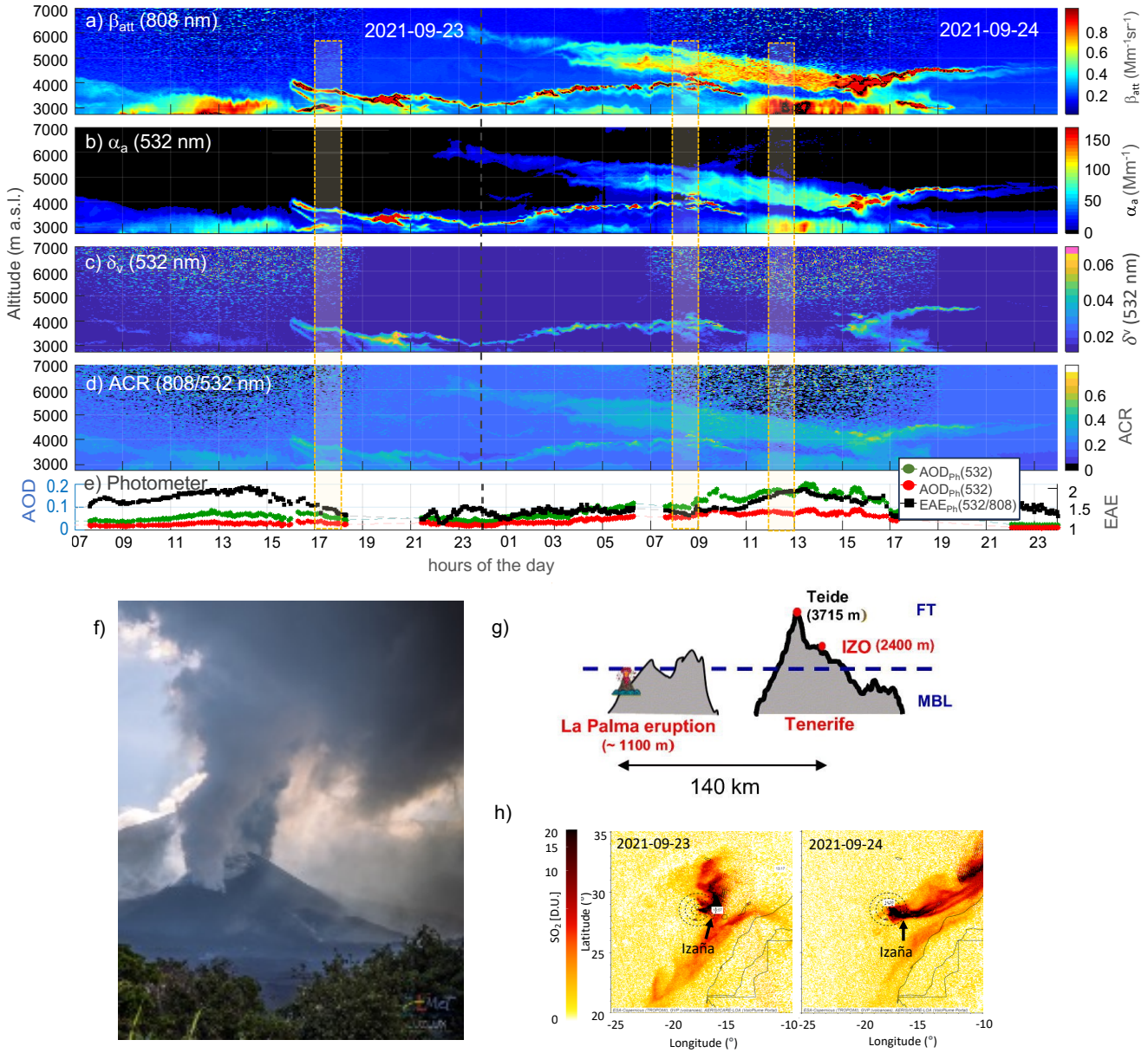

Figure 3. Temporal evolution of a) β_{att} at 808 nm, b) α_a at 532 nm, c) δ^v at 532 nm, d) ACR (808–532) from the CE376, along with e) AOD_{Ph} (532), AOD_{Ph} (808) and EAE_{Ph} (532/808) from the collocated photometer showing the sulfuric volcanic plume over the Izaña Observatory on September 23–24, 2021. Yellow dashed bars in (a)–(e) highlight the time frames selected to calculate the averaged profiles described in Fig. 4. f) Image of the Cumbre Vieja eruption (Courtesy of AEMET). g) Schematic showing the relative location of the Cumbre Vieja volcano and the Izaña Observatory (adapted from Milford et al., 2023). h) Images of TROPOMI SO_2 total vertical column density (in Dobson units, D.U.) from September 23–24, 2021. Images drawn using the VolcPlum interactive portal, developed in the frame of AERIS data center and LOA (https://volcplume.aeris-data.fr/, [accessed July 2, 2024], Boichu and Mathurin, 2022).

For further analysis of the aerosols observed at Izaña, we selected three-time frames (T1, T2, T3) of one to two hours average, that improves the signal-to-noise ratio (SNR) and results in more reliable information (Fig. 4). The aerosol properties presented in Fig. 4 (from left to right) are δ^{v} (532, 808), δ^{p} (532, 808), α_a (532 and 808), β_a (532 and 808), EAE (532/808) from the CE376 and the collocated photometer and CR (808-532) and ACR (808-532). The analysis of the results is presented below:

(a) T1 (2021-09-23 17:00 to 18:00 UTC, Fig. a): the retrieved LR at both wavelengths were 61±10 sr at 532 nm and 76±19 sr at 808 nm, both affected by large errors due to low aerosol loading (AOD_{Ph} (532) =0.07). The LR at 808 nm was retrieved using an estimated AOD at 808 nm and the forward integration Klett method to reduce the uncertainty due to the increasing background noise caused by solar radiation (Sanchez-Barrero et al., 2024). Two well-defined layers of approximately 0.4 km width were detected at 3 km and 3.8 km asl, respectively. The lower layer presented higher extinction (α_a (532) ~115 Mm^{-1}, α_a (808) ~45 Mm^{-1}) than the layer at higher altitude ((α_a (532) ~60 Mm^{-1} and α_a (808) ~48 Mm^{-1}). β_a peak values were ~1.4–1.9 $Mm^{-1}sr^{-1}$ at 532 nm and ~0.6–0.8 $Mm^{-1}sr^{-1}$ at 808 nm. δ^{p} (532) ranges between 0.01 and 0.015, and slightly higher values at 808 nm (0.015–0.02) at the peaks of the layers. The derived EAE_{Lid} was similar to that from the photometer (EAE_{Ph} (532/808) = 1.58), and ACR (808-532) was <0.35. ACR was lower than 0.5, with a large uncertainty (~20%), in relation to the retrieved LR error propagation. Similar uncertainties were also found in EAE. Although the errors were significant, both layers exhibited a predominance of fine spherical aerosols, with a higher contribution in the lower layer compared to the higher layer. At Cabo Verde, south of the volcano, Raman lidar measurements at 532 nm on September 24, 2021, revealed a similarly enhanced lidar ratio of 60.2±9.2 sr within the sulfate-dominated planetary boundary layer, where the sulfate mass concentration was 133.1±20.3 μg m^{-3}). The measurements showed a higher α_a (532) of 549±38 Mm^{-1} within a more aerosol-loaded layer (AOD of 0.43±0.02) compared to those measured at Izaña while, δ^{p} (532) remained within the range 0.007±0.001. These findings suggest a stronger influence of the sulfuric volcanic plume at Cabo Verde on that day, with a predominance of fine-mode aerosols within a more aerosol-loaded layer (Gebauer et al., 2024) (Fig. 3h).

(b) T2 (2021-09-24 08:00 to 09:00 UTC, Fig. b): the retrieved LR at both wavelengths were 39±5 sr at 532 nm and 61±10 sr at 808 nm. This set of profiles revealed 3 thin aerosol layers (~100 m width) between 3.6 and 4.2 km a.s.l., all three with similar extinction coefficients, around ~60 Mm^{-1} at 532 nm and ~40 Mm^{-1}at 808 nm, and similar δ^{p} values around 0.1. Immediately above, a wider layer between 4.3 and 5.3 km asl was detected, with α_a ~60 Mm^{-1} at 532 nm and ~35 Mm^{-1}at 808 nm, β_a ~0.8-1.5 $Mm^{-1}sr^{-1}$ at 532 nm and ~0.6 $Mm^{-1}sr^{-1}$ at 808 nm, and δ^{p} considerably lower (0.03). In contrast EAE_{Lid}, ACR (808-532) and CR (808-532) were likely constant within the 4 layers, all showing values related to the presence of fine aerosols. In particular, the wider layer yields the unique presence of non-ash particles, most likely sulfate aerosols.

(c) T3 (2021-09-24 12:00 to 13:00 UTC, Fig. c): the LR retrieved at both wavelengths were 36±2 sr at 532 nm and 57±7 sr at 808 nm. This set of profiles, follow the descent of the layer centered at 4.8 km asl detected in T2, now placed between 4 and 5 km asl with higher aerosol concentration at 532 nm (extinction: 74 Mm^{-1} at 532 nm and ~40 Mm^{-1} at 808 nm) and δ^{p} values of 0.02. A layer below 3.5 km asl was also detected with higher values of aerosol extinction (100 Mm^{-1} at 532 nm and ~50 Mm^{-1} at 808 nm) and backscatter coefficients (β_a (532) ~2.1–2.9 $Mm^{-1}sr^{-1}$, β_a (808) ~0.6–0.8 $Mm^{-1}sr^{-1}$); and δ^{p} below 0.04. Both layers showed high values of EAE_{Lid} (1.4 and 2, respectively). The ACR (808-532) remained similar in the three cases shown (~0.3–0.4). Thus, an increasing presence of non-ash particles was evidenced, in accordance with the increase of EAE_{Ph} (1.8) with respect to T1 and T2 (1.7 and 1.4, respectively). Similar to dust aerosols, we generally observe slightly higher depolarization values at longer wavelengths.

The analysis presented here indicates the presence of likely non-ash particles (fine and spherical aerosols) at Izaña. This contrast with the more mixed presence of ash and non-ash particles observed when the aerosol profile was measured at 10 km from the volcano on the island of La Palma. There, the lowest and strongest peak of the volcanic plume was observed just above the top of the marine boundary layer (1.3–1.6 km above sea level, according to Sicard et al., 2022; Córdoba-Jabonero et al., 2023). At the start of the volcanic eruption, ash and particulate matter deposition was primarily observed within the marine boundary layer, close to the emission source. Meanwhile, the Izaña station monitored the regional transport at higher altitudes (up to 5 km a.s.l.) of a more dominant fine sulfate particle layer, as these particles can remain suspended for longer periods and travel long distances (Graf et al., 1997).

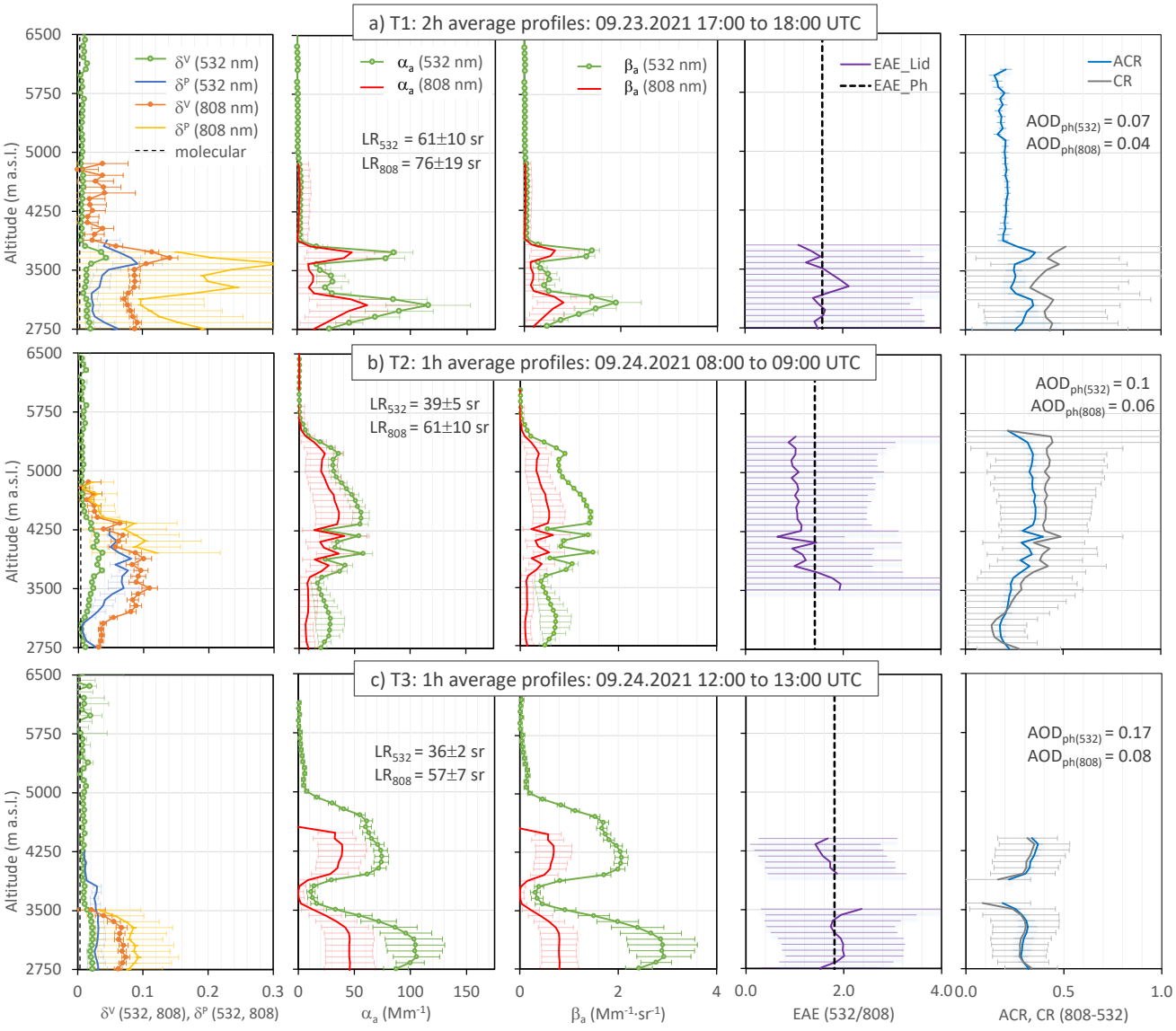

Figure 4. Aerosol properties of the Cumbre Vieja volcanic plume measured at Izaña expressed as average aerosol profiles measured during September 23–24, 2021. Each row represents a 1 h or 2 h profiles including profiles of δ^{v} (532, 808), δ^{p} (532, 808), α_a (532 and 808), β_a (532 and 808) EAE (532/808) from the CE376 and the collocated photometer (EAE_{Lid} and EAE_{Ph}, respectively) and CR (808-532) and ACR (808-532). The selected time frames shown here are highlighted as yellow dashed bars in Fig. 3a–e.

3.2.3 Wildfire aerosols

3.2.3.1 Aged aerosols from Canadian wildfires

Starting in March 2023, Canada suffered from the record-breaking wildfires affecting 15 million hectares of land and with a total emission of carbon of 647 TgC by September 2023 (Byrne et al., 2024). Smoke plumes travelled all over the Atlantic, reaching the Canary Islands within approximately 10 days during May and June 2023. Examples on how these smoke plumes travelled over the Atlantic and reached the Izaña Observatory over these months are shown in Fig. 5a–e and Fig. 6a–e. The

figures include measurements of β_a (808), α_a (532), δ^v (532), ACR (808-532), as well as AOD and EAE_{Ph} from the collocated photometer recorded in May 20–21, 2023 and July 01–02, 2023. These days were chosen to minimize or avoid the simultaneous interaction with Saharan dust particles.

During May 20–21, 2023, a plume of aged biomass burning aerosols from Canada was descending from 9 km to 3.5 km a.s.l. and detected at Izaña. The AERONET VSD indicated a single fine mode with an effective radius centered at 0.26 μm (data available in the AERONET website, not shown for brevity), which is slightly higher than the background value of 0.16 μm typically observed at Izaña (Barreto et al., 2022b), and in the order of magnitude of those observed in particles that have undergone aging (Eck et al., 2009; González et al., 2020). As the plume descended to the observatory, its extinction and backscatter properties diminished, while the values of δ^v (532) and ACR (808-532) remained relatively constant (~0.08 and ~0.05, respectively; Fig. 5a–d). By the evening of May 21, 2023, the plume reached the observatory level. The retrieved LR values were 73±5 sr at 532 nm and 97±6 sr at 808 nm. The aerosol properties measured at this level were δ^v (532) ~0.03, δ^p (532) ~0.06, α_a <120 Mm^{-1} at 532 nm and <70 Mm^{-1} at 808 nm, β_a<1.5 $Mm^{-1}sr^{-1}$ at 532 nm and <0.6 $Mm^{-1}sr^{-1}$ at 808 nm, ACR (808/532) ~0.5, and the EAE_{Lid} given by the lidar system ~ 1.5, similar to that given by the photometer (1.43, Fig. 5h).

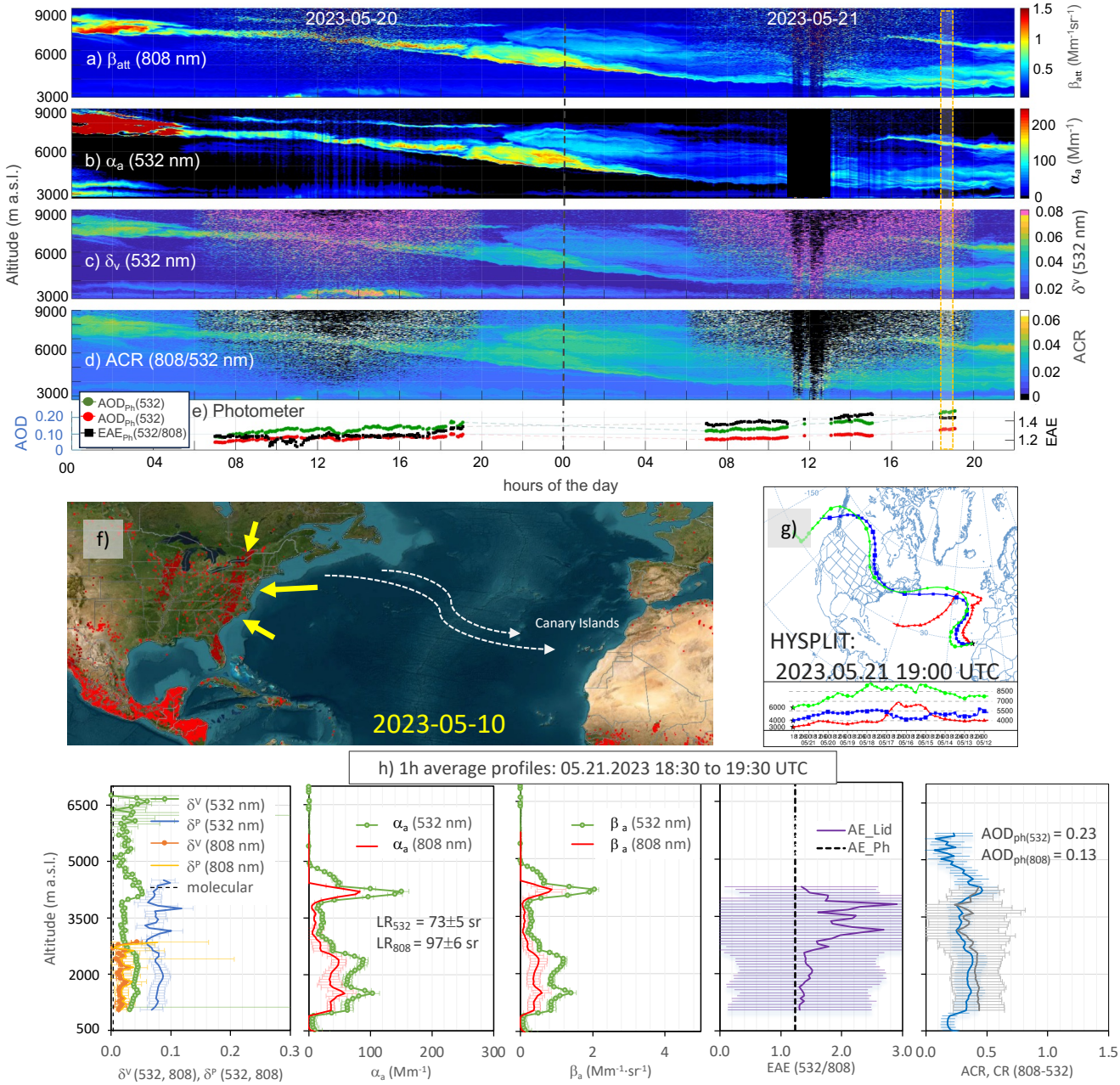

Figure 5. Temporal evolution of a) β_{att} at 808 nm, b) α_a at 532 nm, c) δ^v at 532 nm, d) ACR from the CE376, along with e) AOD$_{Ph}$ (532), AOD$_{Ph}$ (808) and EAE$_{Ph}$ (532/808) from the collocated photometer showing the arrival of long ranged transported (aged) smoke from Canadian wildfires at Izaña Observatory on May 20–21, 2023. f) Satellite images highlighting the Canadian fires (https://firms.modaps.eosdis.nasa.gov, [accessed on June 09, 2024]). g) HYSPLIT isentropic backtrajectories showing the Canadian origin of the airmasses approximately 10 days before the arrival to the Izaña Observatory in the evening on May 20, 2023. h) 1h average profiles of δ^v (532, 808), δ^p (532, 808), α_a (532 and 808), β_a (532 and 808) EAE (532/808) from the CE376 and the collocated photometer (EAE$_{Lid}$ and EAE$_{Ph}$, respectively) and CR (808-532) and ACR (808-532). The selected time frame selected to calculate the averaged profiles in (h) is highlighted as yellow dashed bars in plots (a)–(e).

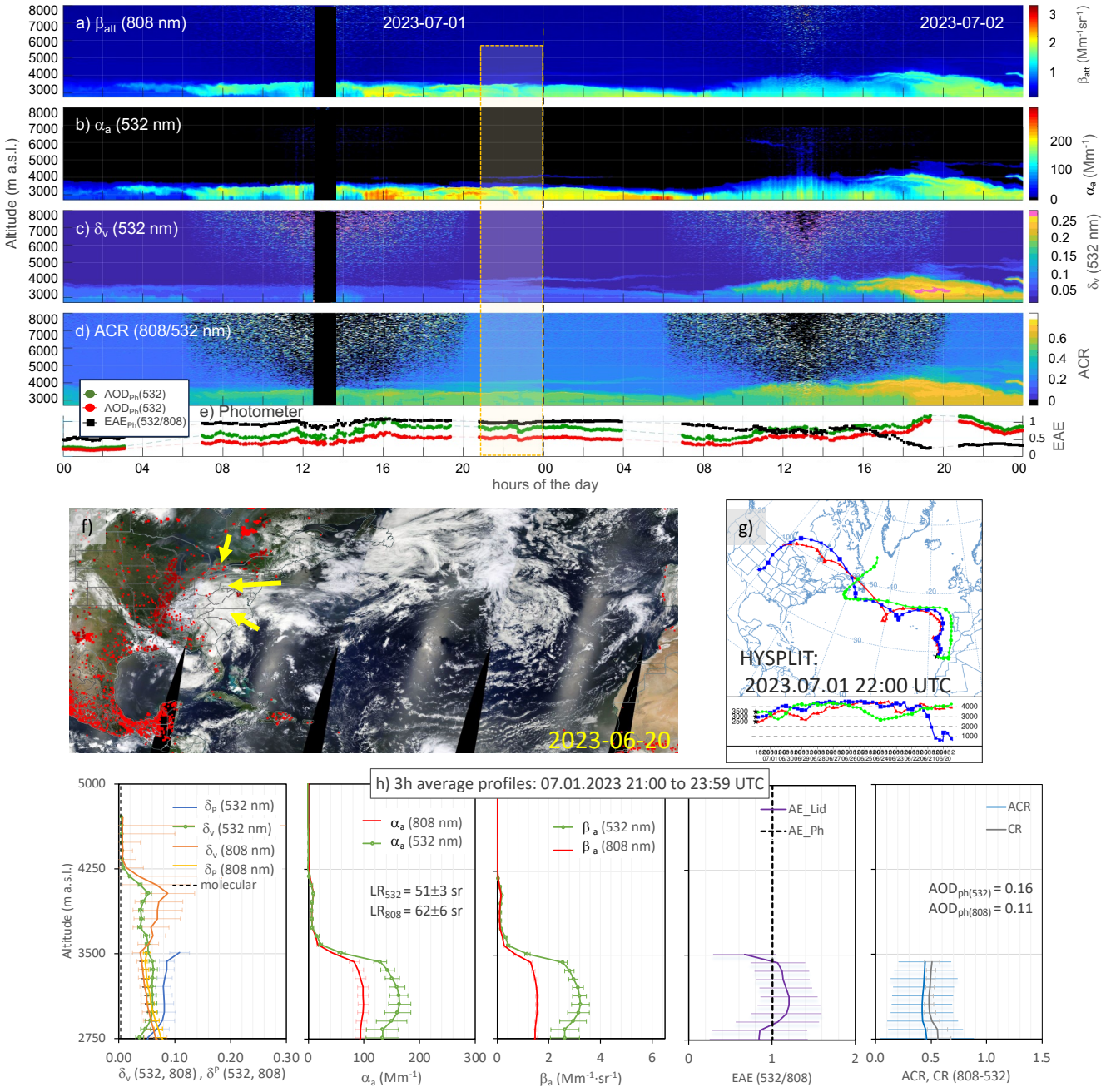

Figure 6. Temporal evolution of a) β_{att} at 808 nm, b) α_a at 532 nm, c) δ^v at 532 nm, d) ACR (808-532) from the CE376, along with e) AOD$_{Ph}$ (532), AOD$_{Ph}$ (808) and EAE$_{Ph}$ (532/808) from the collocated photometer, showing the arrival of long ranged transported (aged) smoke from Canadian wildfires at Izaña Observatory on July 1-2, 2023. f) Satellite images highlighting the Canadian fires (https://firms.modaps.eosdis.nasa.gov) [accessed on June 09, 2024]. g) HYSPLIT isentropic backtrajectories showing the Canadian origin of the airmasses approximately 10 days before the arrival to the Izaña Observatory in the evening of July 1, 2023. h) 3-h

average profiles of δ^v (532, 808), δ^p (532, 808), α_a (532 and 808), β_a (532 and 808) EAE (532/808) from the CE376 and the collocated photometer (EAE_{Lid} and EAE_{Ph}, respectively) and CR (808-532) and ACR (808-532). The selected time frame selected to calculate the averaged profiles in (h) is highlighted as yellow dashed bars in plots (a)–(e).

A new episode of transported smoke was observed by the end of the day of July 1, 2023. This episode presented a minimal influence from the commonly observed summer Saharan dust in comparison to the previous and following days (back trajectories not shown for brevity, Fig. 6a–d). The event was characterized by a quite homogenous layer of aerosols reaching 3.5 km height over Izaña. This layer is characterized by an extinction coefficient of ~149 Mm^{-1} at 532 nm and ~95 Mm^{-1} at 808 nm, backscatter coefficient of ~3 $Mm^{-1}sr^{-1}$ at 532 nm and ~1.5 $Mm^{-1}sr^{-1}$ at 808 nm, ACR (808-532) of 0.4 and δ^p of 0.08 at 532 nm. The EAE_{Lid} (532/808) of 1.14 was slightly higher than that from the photometer. In this event, the AERONET VSD distributions exhibit a bimodal pattern, with a dominant fine mode centered also around 0.26 μm but higher in concentration relative to May, and a coarse mode with lower concentration centered at 1.7 μm (data available in the AERONET website, not shown for brevity). The results shown here, combined with lower retrieved LR (51±3 sr at 532 nm and 62±6 sr at 808 nm) compared to the example shown in Fig. 5, suggest the observation of aged smoke particles, mixed with the remaining contribution of dust aerosols observed the previous and posterior days.

The values of δ^p and retrieved LR at 532 nm obtained in this section fall within the range of those reported in the literature (Gross et al., 2013; Ortiz-Amezcua et al., 2017 and references therein) for Canadian aged Biomass Burning over Europe. The second example presented here shows slightly lower retrieved LR values. Although these lower values are within the expected range, they also indicate a slight mixing with the Saharan dust aerosols, which is more noticeable at longer wavelengths (808 nm). In general, the episodes of Canadian Wildfires smoke show a lower depolarizing effect (δ^v and δ^p at 532 and 808 nm <0.1) and higher EAE due to a more homogenous morphology of the particles in comparison with dust aerosols.

3.2.3.2 Fresh aerosols from forest fires at Tenerife

On August 15, 2023, the island of Tenerife suffered from one of the most devastating fires in recent memory. It began at mid–altitudes and affected over 12,000 hectares largely within the forest. Five days later, on the afternoon of August 20, 2023, the fire reached the Izaña mountain, where the Izaña Observatory is located (Fig. 7h–i). Thanks to the rapid response of firefighting efforts, the observatory's infrastructure was saved. Most of the measurement programs remained operational, recording the historical anomalies during this period.

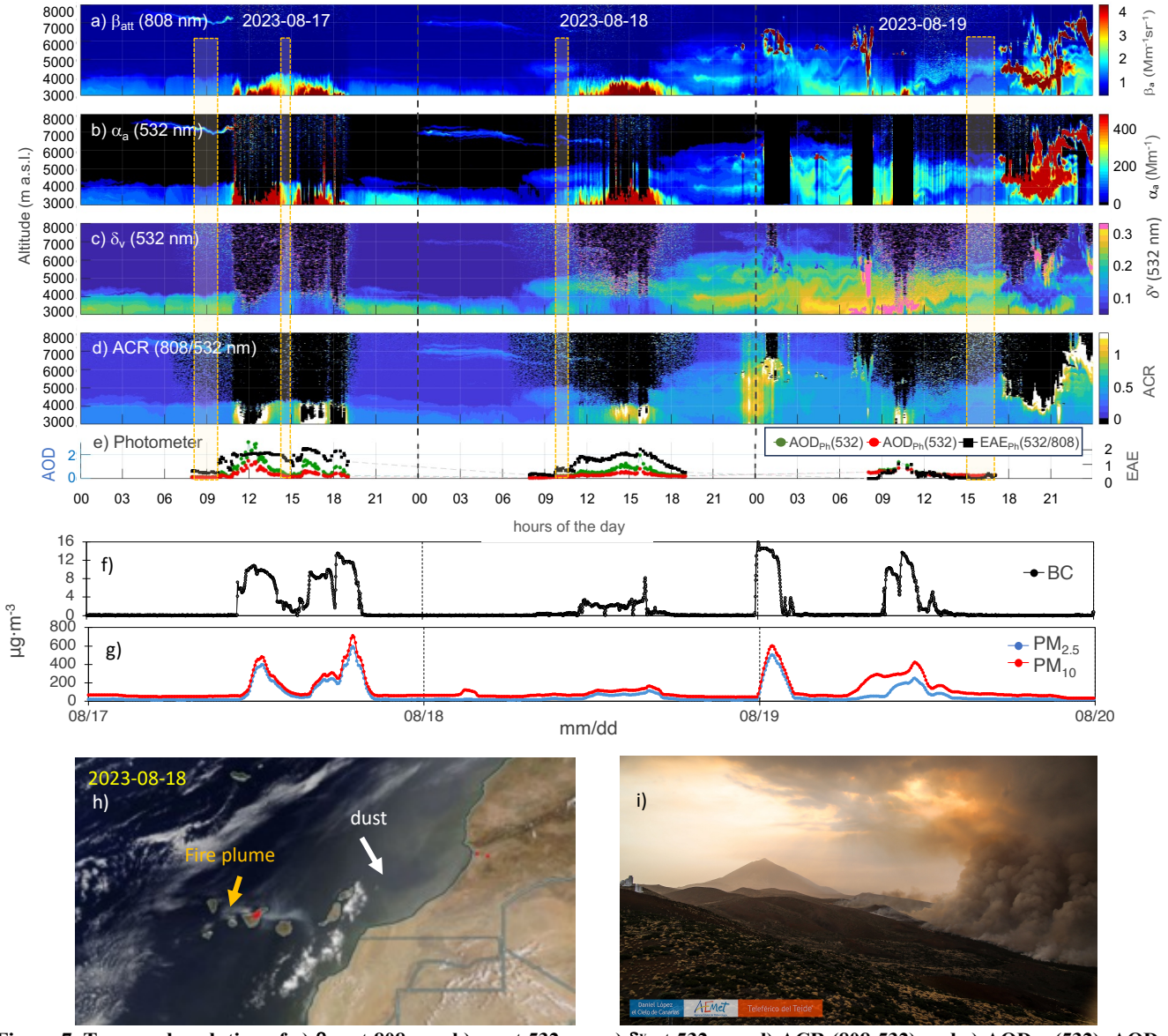

Figure 7. Temporal evolution of a) β_{att} at 808 nm, b) α_a at 532 nm, c) δ^v at 532 nm, d) ACR (808-532) and e) AOD_{Ph} (532), AOD_{Ph} (808) and EAE_{Ph} (532/808) from the collocated photometer showing the arrival of the wildfire smoke from the forestal park in Tenerife at Izaña Observatory in August 17–19, 2023. Yellow dashed bars in (a)–(e) highlight the time frames selected to calculate the averaged profiles described in Fig. 8. f) Black carbon (BC) concentrations measured at 1 μm size cut (PM_1) with a MAAP (Thermo™ at 637 nm) at Izaña. g) Particle matter concentrations measured at 2.5- and 10 μm size cut ($PM_{2.5}$ and PM_{10}) with a 1405-DF (Thermo Fisher Scientific) at Izaña. h) Satellite images highlighting the wildfire at Tenerife and the dispersion plume (https://firms.modaps.eosdis.nasa.gov) [accessed on June 13, 2024]. i) Image of the Teide National Park taken on August 19, 2023, from Izaña Observatory (Teide Cloud Laboratory Project, #TeideLab, Courtesy of AEMET).

Measurements of β_{att} at 808 nm, α_a at 532 nm, δ^v at 532 nm, ACR (808-532) from the CE376, along with the AOD and EAE_{Ph} from the collocated photometer, show the arrival of the local wildfire smoke at Izaña during August 17–19, 2023, (Fig. 7a–e). On the evening of August 18, 2023, and the following days, the trajectories of the air masses and satellite images indicated the

presence of Saharan dust particles and cloudy conditions at Izaña. In addition, when the fire was surrounding the observatory on the evening of August 20, 2023, the virulence of the fire was translated into saturated signals of lidar and photometer systems, making impossible the retrieval of aerosols properties at this stage.

In the previously shown study cases, we used AERONET AOD Level 2.0 to retrieve the aerosol properties. However, in this case, we used AOD level 1.0 because, due to the intensity of the event, most of the photometric measurements were incorrectly screened by AERONET control algorithms and attributed to the presence of clouds, as happened during the desert dust outbreak in February 2020 (Cuevas et at., 2021). To ensure the retrieval of aerosol properties under clear sky conditions, we used 1-minute collocated measurements of global and diffuse short-wave downward radiation (García et al., 2019), following the methodology proposed by Long and Ackerman (2000) and adapted by García et al., (2014) to suit the specific conditions at Izaña. Higher values of β_{att} (808) and α_a (532), along with lower δ^v (532) and ACR (808-532), and an AE close to 2, were particularly observed in the afternoon, especially on August 17 and 18, 2023. This phenomenon was driven by the upslope winds, which are active during daylight hours, transporting burned material upward from the lower forest (1300–1500 m). On August 19, 2023, with the fire getting closer to the observatory and with the influence of Saharan dust conditions (Fig. 7h–i), the measured aerosol showed lower values of β_{att} (808) and α_a (532), higher δ^v (at 532, >0.25) and EAE_{Ph} dropped close to 0.

We selected four time frames (T1–T4; Fig. 8) covering the different aerosol scenarios shown in Fig. 7 and we analyzed the aerosol properties of this event using average profiles of δ^v (532, 808), δ^p (532, 808), α_a (532 and 808), β_a (532 and 808), EAE (532/808) from the CE376 and the collocated photometer, and CR (808-532) and ACR (808-532). The results are presented below:

(a) T1 (2023-08-17 08:00 to 09:30 UTC, Fig. 8a): the retrieved LR were 53±2 sr at 532 nm and 71±2 sr at 808 nm for AOD of 0.15 and 0.11, respectively. During the early hours as well as in the evening, a quite homogeneous layer up to 4.5 km height was observed. This layer presented α_a values of ~85 Mm^{-1} at 532 nm and ~75 Mm^{-1} at 808 nm, β_a of ~1.5 $Mm^{-1}sr^{-1}$ and ~1 $Mm^{-1}sr^{-1}$ at 532 nm and 808 nm, and δ^p (532) of 0.35. EAE_{Lid} (532/808) of ~0.4, like that from the photometer, and ACR values ~ 0.35. This aerosol layer defined the background aerosol levels of the wildfire measured at Izaña and originated at 1000–1500 m lower than the station.

(b) T2 (2023-08-17 14:45 to 15:00 UTC, Fig. 8b): we observed an increase in AOD, EAE (532/808) ~1.3 and α_a (~150 Mm^{-1} and ~85 Mm^{-1} at 532 and 808 nm), and β_a (~3.7 $Mm^{-1}sr^{-1}$ and ~2 $Mm^{-1}sr^{-1}$ at 532 and 808 nm) coefficients, along with a lower depolarization (δ^p (532) ~0.15), with the activation of the upslope flow winds during daylight hours. The retrieved LR were lower, 42±2 sr at 532 nm and 45±2 sr at 808 nm. This indicated the arrival of freshly burned material at the station, carried upward by the wind.

(c) T3 (2023-08-18 08:00 to 09:30 UTC, Fig. 8c): With the evolution of the days, the wildfire extended to higher altitudes, getting closer to the station. In the morning of August 18, 2023, we observed a thicker layer, reaching 5.5 km, characterized by retrieved LR of 51±3 sr at 532 nm and 65±3 sr at 808 nm, and AOD of 0.23 and 0.17 at 532 nm and 808 nm, respectively. It also showed higher δ^p (532) and lower β_a and α_a signals relative to the previous morning. The layer was characterized by an EAE_{Lid} (532/808) of ~0.75 close to that given by the photometer. The arrival of freshly burned material to the station, transported by upslope winds, was also detected that day.

(d) T4 (2023-08-19 15:00 to 17:00 UTC, Fig. 8d): On August 19, 2023, the coupling of two aerosol layers, reaching a total height of 6 km, was observed. These layers were characterized by higher AOD and depolarization values (δ^p (532) >0.3), compared to the previous days. Additionally, the second layer presented higher β_a and α_a signals around 4.5 km. The retrieved LR of 59±2 sr at 532 nm and 86±2 sr at 808 nm for AOD of 0.32 and 0.29, respectively. These observations were attributed to the combined effects of advancing fire towards the observatory and the arrival of Saharan dust particles (air masses not shown for brevity).

During the FIREX-AQ campaign, a similar lidar system prepared for mobile applications, showed comparable ranges of values for retrieved LR, δ^p (532), EAE (532/808), and ACR (808-532). However, it recorded higher extinction and backscatter coefficients, which could be related to their measurement of aerosols predominantly in the fine mode and the intensity of the wildfire and fuel available (Sánchez-Barrero et al., 2024). On the other hand, the extinction, backscatter levels and retrieved LR found here are in the range of those measured by Alados-Arboledas et al. (2011) in fresh biomass burning aerosols. The examples presented here showed overall quite homogeneous layers of δ^v (532, 808) between 0.1–0.2 and ACR (808-532)

between 0.3–0.5. These results suggest well-mixed layers of fine and coarse smoke aerosols of varying sizes and shapes from the forested area. This is consistent with the ash, soot, and charred vegetation that surrounded the observatory during the event, as measured by the in-situ instrumentation at Izaña Observatory. During the wildfire, black carbon concentrations (BC) measured with a PM_1 size cut (1 μm) reached the highest levels ever recorded at Izaña, 16,000 ng m^{-3} (Fig. 7f, MAAP instrument – Thermo™ at 637 nm, background levels <100 ng m^{-3}). The particle matter concentrations at 2.5 and 10 μm size cut ($PM_{2.5}$ and PM_{10}) measured with a TEOM 1405-DF (Thermo Fisher Scientific), reached values of 600 and 700 μg m^{-3}, respectively (Fig. 7g). A closer range between $PM_{2.5}$ and PM_{10} concentrations during August 17 and 18, and more distancing values on the 19th, also described the transition between the observation of more pure wildfire aerosol emissions in the first two days and the mixture with dust aerosols by August 19, 2023 (Fig. 7).

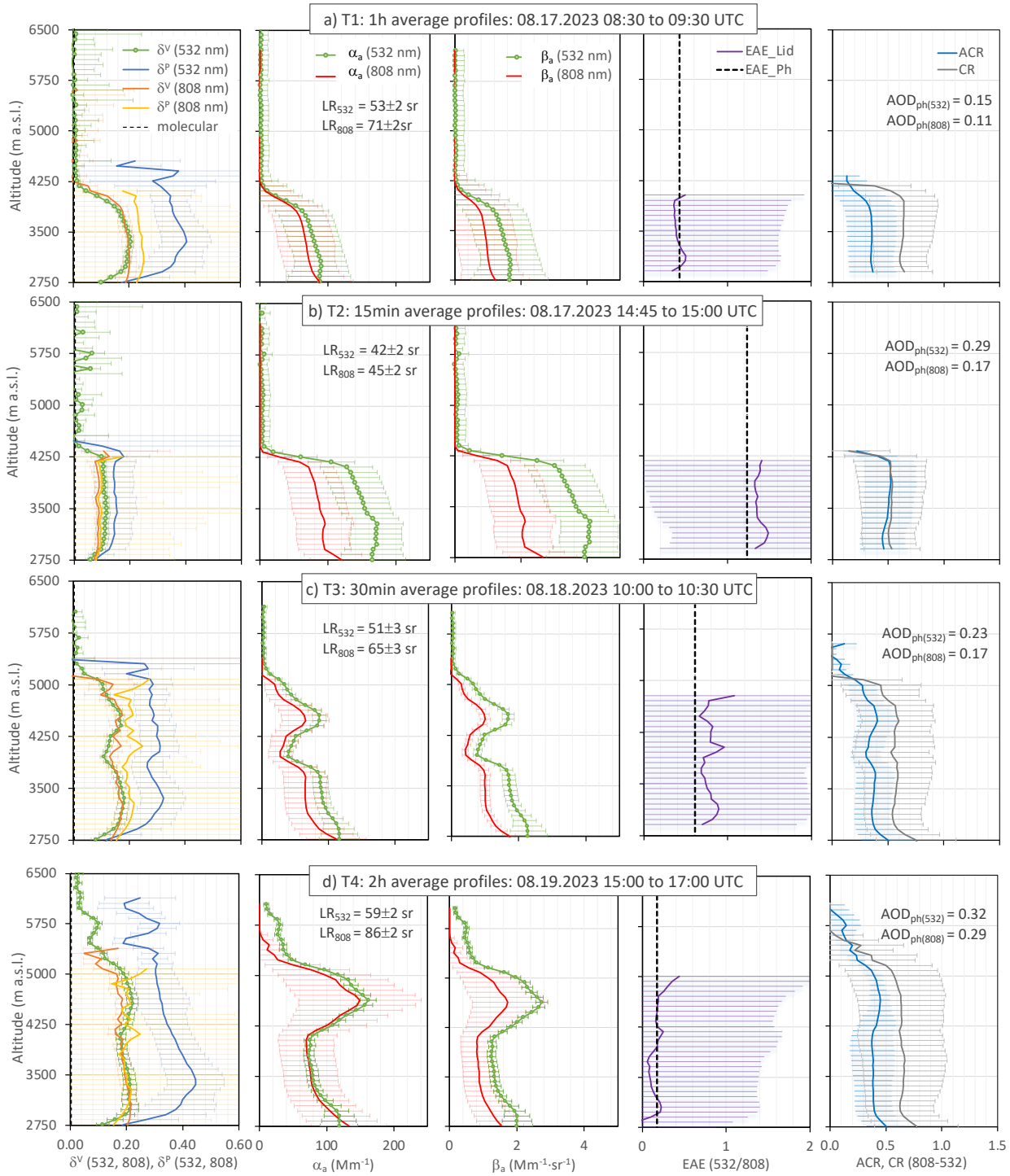

Figure 8. Average aerosol profiles of δ^v (532, 808), δ^p (532, 808), α_a (532 and 808), β_a (532 and 808), EAE (532/808) from the CE376 and the collocated photometer (EAE_{Lid} and EAE_{Ph}, respectively) and CR (808-532) and ACR (808-532) showing the influence of the local wildfires in the aerosol properties measured at Izaña during August 17–19, 2023. The selected time frames shown here are highlighted as yellow dashed bars in the in Fig. 7a–e.

3.3 Aerosol classification

A summary of the retrieved aerosol properties of the events studied in the previous section is shown in Table 1. Fresh Saharan dust particles exhibited the lowest EAE_{Lid} (532/808) (0.30±0.16) and relatively high δ^p (532) values of 0.20±0.01, indicating that they were the largest particles in this study and had non-spherical morphology. Similar values of retrieved LR (532) and δ^v (532) have been reported in literature (Sanchez-Barrero et al., 2024; Barreto et al., 2022b; Gross et al., 2013; Tesche et al., 2011; Tesche et al., 2009a; Tesche et al., 2009b) as well as for δ^p (532) (Haarig, et al., 2022; Gross et al., 2011; Gross et al., 2013). Higher δ^v values at 808 nm relative to those at 532 nm (δ^v (808) = 0.25±0.02), highlight the greater depolarizing and more efficient scattering effect of large non-spherical fresh dust particles at higher wavelengths. Dust also exhibited the highest ACR (808-532) values of 0.54±0.08 compared to the other studied emission sources, consistent with previous reported results (Sanchez-Barrero et al., 2024; Comeron et al., 2017).

Fresh emissions from the local forest fires on the island showed a slightly higher EAE (532/808) (0.68±0.53), lower ACR (808-532) (0.40±0.07) and higher δ^P (532) (0.30±0.11). Comparable values using a similar lidar system were observed during the FIREX-AQ campaign (Sánchez-Barrero et al., 2024). Extinction and backscatter coefficients and retrieved LR measured at 532 nm are also in the range of those from fresh biomass burning aerosols shown by Alados-Arboledas et al. (2011). As discussed in Sect. 3.2.3.2, these aerosols appeared to be a homogeneous mixture of different aerosol types and sizes, consistent with the presence of ash, soot, and charred vegetation in the observatory, which explain the higher particle depolarization ratio for the mixture.

Long-range transported (aged) aerosols from the Canadian biomass burning, observed at the station after a 10-day journey across the Atlantic Ocean, presented values of EAE (532/808) between 1 and 1.3, and relatively low depolarization (δ^P (532) of 0.08±0.01, δ^P (808) of 0.02±0.01). These values describe small particles with a quite homogeneous (spherical) morphology and agree with those previously reported during the observations of Canadian aged Biomass Burning aerosols over Europe (Gross et al., 2013; Ortiz-Amezcua et al., 2017 and references therein). The ACR (808-532) in these events were similar to those measured during the fresh local forest fires (0.44±0.01). We also observed a slight increase in the fine mode and the emerge of a second mode centered at 1.7 μm in the second event shown, suggesting aerosol ageing along the month as suggested by previous studies (Eck et al., 2009; González et al., 2020) together with the mix of trace contributions of dust aerosols observed around the event. The influence of dust is observed in the 808 nm channel, with δ^P increasing from 0.02 to 0.05.

Finally, δ^P (532, 808) of 0.03±0.01, EAE (532/808) of 1.48±0.02, and an ACR (808-532) of 0.3±0.02, describe the small, non-depolarizing sulfate aerosols from the initial days of the Cumbre Vieja volcano eruption. While ash and particulate matter deposition was primarily observed within the marine boundary layer (Sicard et al., 2022; Córdoba-Jabonero et al., 2023) in the surroundings of the volcano, Izaña monitored the typical regional transport of a more dominant fine sulfate particle layer (Graf et al., 1997).

We observe a good agreement between the EAE shown here and those compiled by Floutsi et al. (2023). As pointed by the results and shown in previous studies (Gross et al., 2013), particle linear depolarization ratio is a key measurement for aerosol classification, well differentiating aerosol types. In contrast, while sun photometers can help constrain lidar ratios more effectively, these ratios are still insufficient for aerosol typing when using alone. This is also the case for aerosol classification using aerosol extinction or attenuated backscatter coefficients. It is important to highlight the smaller range of values of the encountered ACR and the similar values obtained for aged and fresh wildfire emissions, but distinguishable from other aerosols sources (Fig. 9a, c–d). In addition, longer wavelengths (such as 808 nm in this case) appear to be more efficient of distinguishing aerosol types and mixtures, particularly when Saharan dust particles are involved due to their heterogeneous morphology (Fig. 9c–d). Using a two-wavelength elastic lidar system, we can combine direct measurements, such as ACR (808-532), with retrieved properties such as δ^P or EAE, to obtain information of the size and composition of the aerosols observed in the four aerosol types studied in this work. The results are consistent with those obtained by combining two retrieved properties such as δ^P or EAE (532/808).

Table 1. Variability of the aerosol properties observed in the four aerosol types studied in this work. The table includes mean and standard deviation of the following parameters: retrieved LR, EAE (532/808), δ^p (532, 808), δ^v (532, 808), β_a (532, 808), α_a (532, 808) and ACR (808-532). The "aged Canadian wildfires" corresponds to the event of May 2023. "Aged Canadian wildfires + dust" corresponds to the mixing event observed in June 2023 that also received a small influence of Saharan dust particles.

Events Aerosol retrieval	Fresh Saharan dust	Fresh volcanic emissions	Fresh forest fires	Aged Canadian wildfires	Aged Canadian wildfires + dust
LR (532) (sr)	58±8	40.7±5.7	51.3±7.04	73±5	51±3
EAE (532/808)	0.210±0.04	1.50±0.28	0.69±0.53	1.43±0.11	1.14±0.05
δ^p (532)	0.30±0.01	0.04±0.02	0.29±0.11	0.08±0.01	0.08±0.01
δ^v (532)	0.15±0.03	0.02±0.01	0.16±0.04	0.04±0.01	0.06±0.01
δ^p (808)	0.31±0.01	0.10±0.06	0.19±0.07	0.02±0.01	0.05±0.01
δ^v (808)	0.25±0.02	0.08±0.02	0.15±0.05	0.02±0.01	0.05±0.01
β_a (532) ($Mm^{-1}sr^{-1}$)	1.78±0.31	2.01±0.48	2.62±0.51	1.41±0.27	2.96±0.32
β_a (808) ($Mm^{-1}sr^{-1}$)	1.01±0.39	0.64±0.14	1.09±0.39	0.51±0.11	1.426±0.09
α_a (532) (Mm^{-1})	70.33±22.04	58.46±22.1	101.41±36.70	67.61±17.46	152.41±11.97
α_a (808) (Mm^{-1})	62.84±23.09	27.87±9.41	74.54±19.92	37.44±10.29	94.45±5.82
ACR (808-532)	0.54±0.08	0.48±0.28	0.40±0.07	0.35±0.02	0.43±0.01

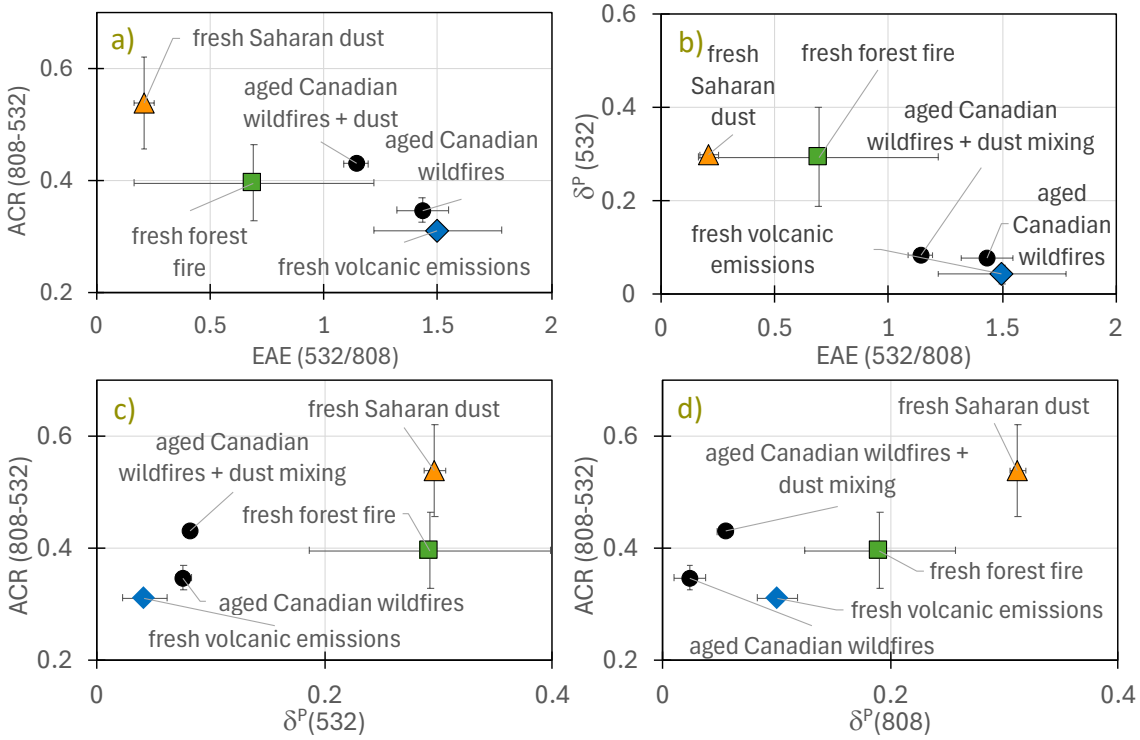

Figure 9. Variability of δ^p (532, 808), ACR (808-532) and EAE (532/808) observed across the different aerosol types studied in this work: 1) fresh Saharan dust particles (orange triangle), 2) fresh emission of volcanic sulfate aerosols (blue rhomboid), 3) aged smoke from Canadian wildfires (black dots) and 4) fresh emissions from local forest fires (green square). Figures a) through d) illustrate the following relationships: a) EAE (532/808) vs. ACR (808-532), b) EAE (532/808) vs. δ^p (532), c) δ^p (532) vs. ACR (808-532), and d) δ^p (808) vs. ACR (808-532).

4 Conclusions

A two-wavelength CE376 micro-lidar (CIMEL) located at the facilities of the Izaña Atmospheric Research Centre (Canary Islands, Spain) was used to provide a comprehensive aerosol typing characterization of the recent aerosol events observed in this subtropical North Atlantic region.

We assessed the performance of the CE376 by comparing its retrieved aerosol products with those measured by an MPL-4B (MPLNET) collocated at Izaña. In general, both systems similarly reproduced the vertical aerosol structure. The main absolute differences were related to errors arising from the determination of the overlap function and the depolarization calibration of each instrument and the larger effect of the solar background on the CE376 system, especially during the central hours of the day, when the analysis is limited to the first 2 km of the atmosphere in the 808 nm channels. By studying the absolute differences in 15-minute profiles, we observed a bias of 0.3% in δ^{v}. The absolute differences on α_a and β_a, measured at 532 nm, were 0.1±0.3 Mm^{-1} and 0.14±0.12 $Mm^{-1}sr^{-1}$, respectively, using the first 4 km of the profile (6.5 km a.s.l) and the full-day dataset. The absolute differences reduced when only nighttime data was considered, with results extended to 10 km a.g.l. The intercomparison with the MPL-4B is presented primarily to highlight the capabilities of an equivalent elastic micro-pulse lidar and to demonstrate the added value of the CE376, which offers two wavelengths and depolarization for aerosol studies. Both the CE376 and MPL lidars are earlier versions of current micro-pulse lidars. An improved design of the CE376 is now available, and the mini-MPL biaxial system has become the standard instrument within the MPLNET network. A dedicated intercomparison campaign between CE376 and MPL using the latest model of the CE376 is planned for the future.

We evaluated the vertical distribution and temporal evolution of different types of aerosols observed at the site, using the additional information provided by the two channels (532, 808 nm) of the CE376. While this mountaintop site is usually known for its pristine, dust-free conditions, it recently experienced the disruptions of three distinct types of aerosol events. Firstly, Saharan dust outbreaks regularly pass over the site towards the Atlantic especially during the summer months. Secondly, the eruption of the Cumbre Vieja Volcano (La Palma, Canary Islands) in September 2021. Lastly, a devastating wildfire occurred in Tenerife in August 2023. Additionally, aerosols transported over long distances from the Canadian wildfire plumes in May and June 2023 were also identified at the site. We showed that combined measurements of particle linear depolarization (δ^{P}), extinction Ångstrom exponent (EAE (532/808)) and attenuated color ratio (ACR (808-532)), described the size and composition of the aerosols shown in this work. Fresh Saharan dust particles exhibited the lowest EAE (532/808) (0.30±0.16) and the highest values of ACR (808-532), together with δ^{P} (532) values 0.20±0.01, being the largest particles in this study with non-spherical morphology. Fresh emissions from the local forest fires on the island showed a slightly higher EAE (532/808) (0.68±0.53), lower ACR (808-532) (0.40±0.07) and higher δ^{P} (532) (0.30±0.11), which support the mixture of different aerosol sizes and types, consistent with the presence of ash, soot, and charred vegetation in the site. Long-range transported aerosols from the Canadian biomass burning exhibited larger EAE (532/808) (1–1.3) and relatively low depolarization (δ^{P} (532) of 0.08±0.01), indicating smaller particles with a more spherical morphology. Finally, δ^{P} (532) of 0.03±0.02, EAE (532/808) of 1.48±0.02, and ACR (808-532) of 0.3±0.02, describe the small, non-depolarizing sulfate aerosols from the initial days of the Cumbre Vieja volcano eruption. These results highlight the potential of two-wavelength micro-pulse lidar systems for continuous monitoring of the temporal evolution and vertical distribution of aerosols. They also demonstrate the ability to distinguish different aerosol types by combining particle linear depolarization ratios and attenuated color ratios. This highlights the CE376's capability as a valuable tool for evaluating both the vertical distribution and temporal evolution of atmospheric aerosols.

Upcoming developments for the CE376 aim to upgrade both lasers to more powerful, eye-safe models, enhancing the system's vertical resolution and capabilities, optimizing its operation. The use of two wavelengths will provide more precise information on the size, composition, vertical distribution, and temporal evolution of atmospheric aerosols. Furthermore, when combined with photometric measurements, the enhanced system will offer a valuable opportunity to obtain both columnar and vertically resolved bimodal aerosol microphysical and optical properties through the Generalized Retrieval of Atmosphere and Surface Properties (GRASP) inversion algorithm (Dubovik et al., 2021; 2014). This makes low-cost, dual-wavelength compact lidar systems capable of improving aerosol retrievals, both during the day and night, by leveraging their sensitivity to aerosol shape and vertical distribution. The application of GRASP is currently under study, with findings to be shared in future publications. These advancements highlight that affordable polarization lidar instruments, operating continuously from the ground, are powerful tools for understanding the distribution and characteristics of aerosol particles on both regional and global scales.

Consequently, they can contribute to improve radiative transfer models, reducing uncertainties in global atmospheric models that predict future climate scenarios, and ultimately enhancing our ability to forecast the influence of atmospheric aerosols on climate.

Data availability. The CE376 data as well as the MPL-4B data are available on request from the Izaña WMO-Measurement Lead Centre for aerosols and water vapor remote sensing instruments (MLC). Data from AERONET used in the present study can be obtained from https://aeronet.gsfc.nasa.gov (accessed on May 05, 2024). Data from MPLNET used in the present study can be obtained from https://mplnet.gsfc.nasa.gov/download_tool/ (accessed on Feb 21, 2024). The vertical soundings can be downloaded from http://weather.uwyo.edu/upperair/sounding.html (accessed on March 14, 2024).

Author Contribution. YG did the data analysis and wrote and revised the paper. MFSB actively contributed to the design of the study and data analysis. EJW provided calibrated data of the MPL lidar and contributed to the writing. IP, SV and FAA actively participated in the discussion on the data analysis and calibration. RDG analyzed the collocated global and diffuse short-wave downward radiation data to evaluate the presence of clouds and confirm the use of level 1 AERONET data. AB, PGS, CT and PG contributed to the writing and the paper enrichment. All coauthors provided comments on the paper.

Competing interests. The authors declare no conflict of interest.

Acknowledgements. This work is part of the activities of the WMO-Measurement Lead Centre for aerosols and water vapor remote sensing instruments (MLC). Software developments for data analysis of the CE376 lidar have been performed in the frame the AGORA-Lab initiative (https://www.agora-lab.fr). The AERONET sun photometers at Izaña were calibrated through the AEROSPAIN Central Facility (https://aerospain.aemet.es/, accessed on May 05, 2024). Action under the ACTRIS grant (agreement no. 871115). We gratefully acknowledge the data provided by the AERONET and MPLNet networks. The MPLNET project is funded by the NASA Radiation Sciences Program and Earth Observing System.

References

Adam, M., Fragkos, K., Binietoglou, I., Wang, D., Stachlewska, I. S., Belegante, L., and Nicolae, V.: Towards Early Detection of Tropospheric Aerosol Layers Using Monitoring with Ceilometer, Photometer, and Air Mass Trajectories, Remote Sens., 14, 1217, https://doi.org/10.3390/rs14051217, 2022.

Alados-Arboledas, L., Müller, D., Guerrero-Rascado, J. L., Navas-Guzmásn, F., Pérez-Ramirez, D. and Olmo, F. J.: Optical and microphysical properties of fresh biomass burning aerosol retrieved by Raman lidar, and star-and sun-photometry, Geophys. Res. Lett., 38, L01807, https://doi.org/10.1029/2010GL045999, 2011.

Ångström, A.: On the Atmospheric Transmission of Sun Radiation and on Dust in the Air, Geogr. Ann., 11(2), 156–166, https://doi.org/10.1080/20014422.1929.11880498, 1929.

Ansmann, A., Riebesell, M. and Weitkamp, C.: Measurement of atmospheric aerosol extinction profiles with a Raman lidar, Opt. Lett. 15, 746-748, 1990.

Barreto, Á., Cuevas, E., García, R. D., Carrillo, J., Prospero, J. M., Ilić, L., Basar, S., Berjón, A. J., Marrero, C. L., Hernández, Y., Bustos, J. J., Ničković, S., and Yela,, M.: Long-term characterisation of the vertical structure of the Saharan Air Layer over the Canary Islands using lidar and radiosondes profiles: implications for radiative and cloud processes over the subtropical Atlantic Ocean, Atmos. Chem. Phys., 22, 739-763, https://doi.org/10.5194/acp-22-739-2022, 2022a.

Barreto, Á., García, R. D., Guirado-Fuentes, C., Cuevas, E., Almansa, A. F., Milford, C., Toledano, C., Expósito, F. J., Díaz, J. P., and León-Luis, S. F.: Aerosol characterisation in the subtropical eastern North Atlantic region using long-term AERONET measurements. Atmos. Chem. Phys., 22(17), 11105-11124, https://doi.org/10.5194/acp-22-11105-2022, 2022b.

Bedoya-Velásquez, A. E., Hoyos-Restrepo, M., Barreto, A., García, R. D., Romero-Campos, P. M., García, O., Ramos, R., Roininen, R., Toledano, C., Sicard, M., and Ceolato, R.: Estimation of the Mass Concentration of Volcanic Ash Using

Ceilometers: Study of Fresh and Transported Plumes from La Palma Volcano, Remote Sens., 14(22), 5680, https://doi.org/10.3390/rs14225680, 2022.

Boichu, M. and Mathurin, T.: VOLCPLUME, an interactive web portal for the multiscale analysis of volcanic plume physico-chemical properties [Interactive Web based Ressource], AERIS, https://doi.org/10.25326/362, Portal access: https://volcplume.aeris-data.fr, Website address: https://www.icare.univ-lille.fr/volcplume/, (accessed July 2, 2024), 2022.

Boichu, M., Grandin, R., Blarel, L., Torres, B., Derimian, Y., Goloub, P., Brogniez, C., Chiapello, I., Dubovik, O., Mathurin, T., Pascal, N., Patou, M., and Riedi, J.: Growth and Global Persistence of Stratospheric Sulfate Aerosols From the 2022 Hunga Tonga–Hunga Ha'apai Volcanic Eruption, J. Geophys. Res. Atmos., 128, https://doi.org/10.1029/2023JD039010, 2023.

Boucher, O., Randall, D., Artaxo, P., Bretherton, C., Feingold, G., Forster, P., Kerminen, V.-M., Kondo, Y., H. Liao, Lohmann, U., Rasch, P., Satheesh, S. K., Sherwood, S., Stevens, B., and Zhang, X. Y.: Clouds and Aerosols, in: Climate Change 2013: The Physical Science Basis. Contribution of Working Group I to the Fifth Assessment Report of the Intergovernmental Panel on Climate Change, Cambridge University Press, Cambridge, United Kingdom and New York, NY, USA, 2013.

Bovchaliuk, V., Goloub, P., Podvin, T., Veselovskii, I., Tanre, D., Chaikovsky, A., Dubovik, O., Mortier, A., Lopatin, A., Korenskiy, M., and Victori, S.: Comparison of aerosol properties retrieved using GARRLiC, LIRIC, and Raman algorithms applied to multi-wavelength lidar and sun/sky-photometer data, Atmos. Meas. Tech., 9, 3391–3405, https://doi.org/10.5194/amt-9-3391-2016, 2016.

Byrne, B., 1 Liu, J., Bowman, K. W., Pascolini-Campbell, M., Chatterjee, A., Pandey, s., Miyazaki, K., van der Werf, G. R., Wunch, D., Wennberg, P. O., Roehl, C. M., and Sinha, S., Carbon emissions from the 2023 Canadian wildfires, Nature, https://doi.org/10.1038/s41586-024-07878-z, 2024.

Burton, S. P., Ferrare, R. A., Vaughan, M. A., Omar, A. H., Rogers, R. R., Hostetler, C. A., and Hair, J. W.: Aerosol classification from airborne HSRL and comparisons with the CALIPSO vertical feature mask, Atmos. Meas. Tech., 6, 1397–1412, https://doi.org/10.5194/amt-6-1397-2013, 2013.

Campbell, J. R., Hlavka, D. L., Welton, E. J., Flynn, C. J., Turner, D. D., Spinhirne, J. D., Scott, V. S., and Hwang, I. H.: Full-Time, Eye-Safe Cloud and Aerosol Lidar Observation at Atmospheric Radiation Measurement Program Sites: Instruments and Data Processing, J. Atmos. Oceanic Technol., 19, 431–442, https://doi.org/10.1175/1520-0426(2002)019<0431:FTESCA>2.0.CO;2, 2002.

Carrillo, J., Guerra, J. C., Cuevas, E., and Barrancos, J.: Characterization of the Marine Boundary Layer and the Trade-Wind Inversion over the Subtropical North Atlantic, Bound.-Lay. Meteorol., 158, 311–330, https://doi.org/10.1007/s10546-015-0081-1, 2016.

Cazorla, A., Casquero-Vera, J. A., Román, R., Guerrero-Rascado, J. L., Toledano, C., Cachorro, V., Orza, J. A. G., Cancillo, M. L., Serrano, A., Titos, G., Pandolfi, M., Alastuey, A., Hanrieder, N., Alados-Arboledas, L.: Near-real-time processing of a ceilometer network assisted with sun-photometer data: monitoring a dust outbreak over the Iberian Peninsula, Atmos. Chem. Phys., 17, 11861–11876, https://doi.org/10.5194/acp-17-11861-2017, 2017.

Comerón, A., Muñoz-Porcar, C., Rocadenbosch, F., Rodríguez-Gómez, A., Sicard, M.: Current Research in Lidar Technology Used for the Remote Sensing of Atmospheric Aerosols, Sensors, 17, 1450. https://doi.org/10.3390/s17061450, 2017.

Córdoba-Jabonero, C., Ansmann, A., Jiménez, C., Baars, H., López-Cayuela, M.-Á., and Engelmann, R.: Experimental assessment of a micro-pulse lidar system in comparison with reference lidar measurements for aerosol optical properties retrieval, Atmos. Meas. Tech., 14, 5225–5239, https://doi.org/10.5194/amt-14-5225-2021, 2021.

Córdoba-Jabonero, C., Sicard, M., Barreto, Á., Toledano, C., López-Cayuela, M. Á., Gil-Díaz, C., García, O., Carvajal-Pérez, C. V., Comerón, A., Ramos, R., Muñoz-Porcar, C., and Rodríguez-Gómez, A.: Fresh volcanic aerosols injected in the atmosphere during the volcano eruptive activity at the Cumbre Vieja area (La Palma, Canary Islands): Temporal evolution and vertical impact, Atmos. Environ., 300, 119667, https://doi.org/10.1016/j.atmosenv.2023.119667, 2023.

Cuevas, E., Milford, C., Barreto, A., Bustos, J. J., García, O. E., García, R. D., Marrero, C., Prats, N., Ramos, R., Redondas, A., Reyes, E., Rivas-Soriano, P. P., Romero-Campos, P. M., Torres, C. J., Schneider, M., Yela, M., Belmonte, J., Almansa, F., López-Solano, C., Basart, S., Werner, E., Rodríguez, S., Alcántara, A., Alvarez, O., Bayo, C., Berjón, A., Borges, A., Carreño, V., Castro, N. J., Chinea, N., Cruz, A. M., Damas, M., González, Y., Hernández, C., Hernández, J., León-Luís, S. F., López-Fernández, R., López-Solano, J., Mármol, I., Martín, T., Parra, F., Rodríguez-

Valido, M., Santana, D., Santo-Tomás, F. and Serrano, A.: Izaña Atmospheric Research Center Activity Report 2021-2022. (Eds. Cuevas, E., Milford, C. and Tarasova, O.), State Meteorological Agency (AEMET), Madrid, Spain and World Meteorological Organization, Geneva, Switzerland, NIPO: 666-24-002-7, WMO/GAW Report No. 290, https://doi.org/10.31978/666-24-002-7, 2024.

Cuevas, E., Milford, C., Barreto, A., Bustos, J. J., García, R. D., Marrero, C. L., Prats, N., Bayo, C., Ramos, R., Terradellas, E., Suárez, D., Rodríguez, S., de la Rosa, J., Vilches, J., Basart, S., Werner, E., López-Villarrubia, E., Rodríguez-Mireles, S., Pita Toledo, M. L., González, O., Belmonte, J., Puigdemunt, R., Lorenzo, J.A., Oromí, P., and del Campo-Hernández, R.: Desert Dust Outbreak in the Canary Islands (February 2020): Assessment and Impacts. (Eds. Cuevas, E., Milford, C. and Basart, S.), State Meteorological Agency (AEMET), Madrid, Spain and World Meteorological Organization, Geneva, Switzerland, WMO Global Atmosphere Watch (GAW) Report No. 259, WWRP 2021-1, https://www.aemet.es/documentos/es/conocermas/recursos_en_linea/publicaciones_y_estudios/publicaciones/GAW_Report_No_259/GAW_Report_No_259.pdf (accessed on January 11, 2024), 2021.

Cuevas, E.: Estudio del Comportamiento del Ozono Troposférico en el Observatorio de Izaña (Tenerife) y su Relación con la Dinámica Atmosférica, PhD thesis, Universidad Complutense de Madrid, Madrid, available at: https://eprints.ucm.es/id/eprint/ 1964/ (accessed on September 13, 2024), 1995.

Dos Santos Oliveira, D. C. F., Sicard, M., Rodríguez-Gómez, A., Comerón, A., Muñoz-Porcar, C., Gil-Díaz, C., Lolli, S., Dubovik, O., Lopatin, A., Herrera, M. E., and Herreras-Giralda, M.: Evaluation of the Accuracy of the Aerosol Optical and Microphysical Retrievals by the GRASP Algorithm from Combined Measurements of a Polarized Sun-Sky-Lunar Photometer and a Three-Wavelength Elastic Lidar, Remote Sens., 15, 5010, https://doi.org/10.3390/rs15205010, 2023.

Dubovik, O., Fuertes, D., Litvinov, P., Lopatin, A., Lapyonok, T., Doubovik, I., Xu, F., Ducos, F., Chen, C., Torres, B., Derimian, Y., Li, L., Herreras-Giralda, M., Herrera, M., Karol, Y., Matar, C., Schuster, GL., Espinosa, R., Puthukkudy, A., Li, Z., Fischer, J., Preusker, R., Cuesta, J., Kreuter, A., Cede, A., Aspetsberger, M., Marth, D., Bindreiter, L., Hangler, A., Lanzinger, V., Holter, C. and Federspiel, C.: A Comprehensive Description of Multi-Term LSM for Applying Multiple a Priori Constraints in Problems of Atmospheric Remote Sensing: GRASP Algorithm, Concept, and Applications, Front. Remote Sens. 2:706851, doi: 10.3389/frsen.2021.706851 2021,

Dubovik, O., Lapyonok, T., Litvinov, P., Herman, M., Fuertes, D., Ducos, F., Lopatin, A., Chaikovsky, A., Torres, B., Derimian, Y., Huang, X., Aspetsberger, M., and Federspiel, C.: GRASP: a versatile algorithm for characterizing the atmosphere, SPIE Newsroom. 10.1117/2.1201408.005558, 2014

Dubovik, O., Holben, B., Eck, T. F., Smirnov, A., Kaufman, Y. J., King, M. D., Tanré, D., and Slutsker, I.: Variability of Absorption and Optical Properties of Key Aerosol Types Observed in Worldwide Locations, J. Atmos. Sci., 59, 590–608, https://doi.org/10.1175/1520-0469(2002)059<0590:VOAAOP>2.0.CO;2, 2002.

Dubovik, O. and King, M. D.: A flexible inversion algorithm for retrieval of aerosol optical properties from Sun and sky radiance measurements, J. Geophys. Res., 105, 20673–20696, https://doi.org/10.1029/2000JD900282, 2000.

Eck, T.F, Holben, B.N., Reid, J.S., Sinyuk, A., Hyer, E.J., O'Neill, N.T., Shaw, G.E., Vande Castle, J.R., Chapin, F.S., Dubovik, O., Smirnov, A., Vermote, E., Schafer, J.S., Giles, D., Slutsker, I., Sorokine, M., Newcomb, W.W., Optical properties of boreal region biomass burning aerosols in central Alaska and seasonal variation of aerosol optical depth at an Arctic coastal site, J. Geophys. Res. Atmos., https://doi.org/10.1029/2008JD010870, 2009.

Floutsi, A. A., Baars, H., Engelmann, R., Althausen, D., Ansmann, A., Bohlmann, S., Heese, B., Hofer, J., Kanitz, T., Haarig, M., Ohneiser, K., Radenz, M., Seifert, P., Skupin, A., Yin, Z., Abdullaev, S. F., Komppula, M., Filioglou, M., Giannakaki, E., Stachlewska, I. S., Janicka, L., Bortoli, D., Marinou, E., Amiridis, V., Gialitaki, A., Mamouri, R.-E., Barja, B., and Wandinger, U.: DeLiAn – a growing collection of depolarization ratio, lidar ratio and Ångström exponent for different aerosol types and mixtures from ground-based lidar observations, Atmos. Meas. Tech., 16, 2353–2379, https://doi.org/10.5194/amt-16-2353-2023, 2023.

Flynn, C. J., Mendoza, A., Zheng, Y., and Mathur, S.: Novel polarization-sensitive micropulse lidar measurement technique, Opt. Express, 15, 2785–2790, https://doi.org/10.1364/OE.15.002785, 2007.

Forster, P., Storelvmo, T., Armour, K., Collins, W., Dufresne, J. L., Frame, D., Lunt, D., Mauritsen, T., Palmer, M., Watanabe, M., Wild, M., Zhang, H.: The Earth's Energy Budget, Climate Feedbacks, and Climate Sensitivity. Cambridge University Press, Cambridge, United Kingdom and New York, NY, USA. p. 923–1054, chapter in: Climate Change 2021 – The Physical Science Basis, 2021.

Freudenthaler, V.: About the effects of polarising optics on lidar signals and the Δ90 calibration, Atmos. Meas. Tech., 9, 4181–4255, https://doi.org/10.5194/amt-9-4181-2016, 2016.

Freudenthaler, V., Esselbron, M., Wiegner, M., Heese, B., Tesche, M., Asmann, A., Müller, D., Althausen, D., wirth, M., Fix, A., Ehret, G., Knippertz, P., Toledano, C., Gasteiger, J., Garhammer, M. and Seefeldner, M.: Depolarization ratio profiling at several wavelengths in pure Saharan dust during SAMUM 2006. Tellus, Ser. B Chem. Phys. Meteorol., 61(1), 165–179, https://doi.org/10.1111/j.1600-0889.2008.00396.x, 2009.

García, R. D., Cuevas, E., Ramos, R., Cachorro, V. E., Redondas, A., and Moreno-Ruiz, J. A.: Description of the Baseline Surface Radiation Network (BSRN) station at the Izaña Observatory (2009–2017): measurements and quality control/assurance procedures, Geosci. Instrum. Method. Data Syst., 8, 77-96, https://doi.org/10.5194/gi-8-77-2019, 2019.

García, R. D., García, O. E, Cuevas, E., Cachorro, V. E., Romero-Campos, P. M., Ramos, R. and de Frutos, A. M.: Solar radiation measurements compared to simulations at the BSRN Izaña station. Mineral dust radiative forcing and efficiency study, J. Geophys. Res. Atmos., 119, 179–194, https://doi.org/10.1002/2013JD020301, 2014.

Gasteiger, J. and Freudenthaler, V.: Benefit of depolarization ratio at λ = 1064 nm for the retrieval of the aerosol microphysics from lidar measurements, Atmos. Meas. Tech., 7, 3773–3781, https://doi.org/10.5194/amt-7-3773-2014, 2014.

Gebauer, H., Floutsi, A. A., Haarig, M., Radenz, M., Engelmann, R., Althausen, D., Skupin, A., Ansmann, A., Zenk, C., and Baars, H.: Tropospheric sulfate from Cumbre Vieja (La Palma) observed over Cabo Verde contrasted with background conditions: a lidar case study of aerosol extinction, backscatter, depolarization and lidar ratio profiles at 355, 532 and 1064 nm, Atmos. Chem. Phys., 24, 5047–5067, https://doi.org/10.5194/acp-24-5047-2024, 2024.

Giles, D. M., Sinyuk, A., Sorokin, M. G., Schafer, J. S., Smirnov, A., Slutsker, I., Eck, T. F., Holben, B. N., Lewis, J. R., Campbell, J. R., Welton, E. J., Korkin, S. V., and Lyapustin, A. I.: Advancements in the Aerosol Robotic Network (AERONET) Version 3 database – automated near-real-time quality control algorithm with improved cloud screening for Sun photometer aerosol optical depth (AOD) measurements, Atmos. Meas. Tech., 12, 169–209, https://doi.org/10.5194/amt-12-169-2019, 2019.

González, R., Toledano, C., Román, R., Mateos, D., Asmi, E., Rodríguez, E., Lau, I. C., Ferrara, J., D'Elia, R., Antuña-Sánchez, J. C., Cachorro, V. E., Calle, A., de Frutos, Á. M.: Characterization of Stratospheric Smoke Particles over the Antarctica by Remote Sensing Instruments, Remote Sens., 12(22), 3769; https://doi.org/10.3390/rs12223769, 2020.

Graf, H. F., Feichter, J., Langmann, B.: Volcanic sulfur emissions: Estimates of source strength and its contribution to the global sulfate distribution, J. Geophys. Res. Atmos., 102(D9), 10727-10738, https://doi.org/10.1029/96JD03265, 1997.

Granados-Muñoz, M. J., Guerrero-Rascado, J. L., Bravo-Aranda, J. A., Navas-Guzmán, F., Valenzuela, A., Lyamani, H., Chaikovsky, A., Wandinger, U., Ansmann, A., Dubovik, O., Grudo, J. O., and Alados-Arboledas, L.: Retrieving aerosol microphysical properties by Lidar-Radiometer Inversion Code (LIRIC) for different aerosol types: Microphysical properties by LIRIC, J. Geophys. Res. Atmos., 119, 4836–4858, https://doi.org/10.1002/2013JD021116, 2014.

Groß, S., Esselborn, M., Weinzierl, B., Wirth, M., Fix, A., and Petzold, A.: Aerosol classification by airborne high spectral resolution lidar observations, Atmos. Chem. Phys., 13, 2487–2505, https://doi.org/10.5194/acp-13-2487-2013, 2013.

Groß, S., Tesche, M., Freudenthaler, V., Toledano, C., Wiegner, M., Ansmann, A., Althausen, D., and Seefeldner, M.: Characterization of Saharan dust, marine aerosols and mixtures of biomass- burning aerosols and dust by means of multi-wavelength de- polarization and Raman lidar measurements during SAMUM- 2, Tellus B, 63, 706–724, https://doi.org/10.1111/j.1600-0889.2011.00556.x, 2011.

Haarig, M., Ansmann, A., Engelmann, R., Baars, H., Toledano, C., Torres, B., Althausen, D., Radenz, M., and Wandinger, U.: First triple-wavelength lidar observations of depolarization and extinction-to-backscatter ratios of Saharan dust, Atmos. Chem. Phys., 22, 355–369, https://doi.org/10.5194/acp-22-355-2022, 2022.

Holben, B., Eck, T., Slutsker, I., Tanré, D., Buis, J., Setzer, A., Vermote, E., Reagan, J., Kaufman, Y., Nakajima, T., Lavenu, F., Jankowiak, I., and Smirnov, A.: AERONET – A Federated Instrument Network and Data Archive for Aerosol Characterization, Remote Sens. Environ., 66, 1–16, https://doi.org/10.1016/S0034-4257(98)00031-5, 1998.

Jin, Y., Sugimoto, N., Shimizu, A., Nishizawa, T., Kai, K., Kawai, K., Yamazaki, A., Sakurai, M., and Wille, H.: Evaluation of ceilometer attenuated backscattering coefficients for aerosol profile measurement, J. Appl. Rem. Sens., 12, 1, https://doi.org/10.1117/1.JRS.12.042604, 2018.

Klett, J. D.: Lidar Inversion with Variable Backscatter/Extinction Ratios, Appl. Opt., 24, 1638-1643. https://doi.org/10.1364/AO.24.001638, 1985.

Kusmierczyk-Michulec, J.: Empirical relationships between aerosol mass concentrations and Ångström parameter, Geophys. Res. Lett., 29, 1145, https://doi.org/10.1029/2001GL014128, 2002.

Laj, P., Lund Myhre, C., Riffault, V., Amiridis, V., Fuchs, H., Eleftheriadis, K., Petäjä, T., Salameh, T., Kivekäs, N., Juurola, E., Saponaro, G., Philippin, S., Cornacchia, C., Alados Arboledas, L., Baars, H., Claude, A., De Mazière, M., Dils, B., Dufresne, M., Evangeliou, N., Favez, O., Fiebig, M., Haeffelin, M., Herrmann, H., Höhler, K., Illmann, N., Kreuter, A., Ludewig, E., Marinou, E., Möhler, O., Mona, L., Eder Murberg, L., Nicolae, D., Novelli, A., O'Connor, E., Ohneiser, K., Petracca Altieri, R., Picquet-Varrault, B., van Pinxteren, D., Pospichal, B., Putaud, J., Reimann, S., Siomos, N., Stachlewska, I., Tillmann, R., Voudouri, K., Wandinger, U., Wiedensohler, A., Apituley, A., Comerón, A., Gysel-Beer, M., Mihalopoulos, N., Nikolova, N., Pietruczuk, A., Sauvage, S., Sciare, J., Skov, H., Svendby, T., Swietlicki, E., Tonev, D., Vaughan, G., Zdimal, V., Baltensperger, U., Doussin, J., Kulmala, M., Pappalardo, G., Sorvari Sundet, S. and Vana, M.: Aerosol, Clouds and Trace Gases Research Infrastructure (ACTRIS): The European Research Infrastructure Supporting Atmospheric Science. Bulletin of the American Meteorological Society 105(7) pp. E1098-E1136, 2024. Available at: https://journals.ametsoc.org/view/journals/bams/105/7/BAMS-D-23-0064.1.xml, [Accessed 30 Jan 2025].

Li, D., Wu, Y., Gross, B., and Moshary, F.: Capabilities of an Automatic Lidar Ceilometer to Retrieve Aerosol Characteristics within the Planetary Boundary Layer, Remote Sens., 13, 3626, https://doi.org/10.3390/rs13183626, 2021.

Long, C. N. and Ackerman, T. P.: Identification of clear skies from broadband pyranometer measurements and calculation of downwelling shortwave cloud effects, J. Geophys. Res., 105, 15,609–15,626, https://doi.org/10.1029/2000JD900077, 2000.

Lopatin, A., Dubovik, O., Fuertes, D., Stenchikov, G., Lapyonok, T., Veselovskii, I., Wienhold, F. G., Shevchenko, I., Hu, Q., and Parajuli, S.: Synergy processing of diverse ground-based remote sensing and in situ data using the GRASP algorithm: applications to radiometer, lidar and radiosonde observations, Atmos. Meas. Tech., 14, 2575–2614, https://doi.org/10.5194/amt-14-2575-2021, 2021.

Lopatin, A., Dubovik, O., Stenchikov, G., Welton, E. J., Shevchenko, I., Fuertes, D., Herreras-Giralda, M., Lapyonok, T., and Smirnov, A.: Comparison of diurnal aerosol products retrieved from combinations of micro-pulse lidar and sun photometer observations over the KAUST observation site, Atmos. Meas. Tech., 17, 4445–4470, https://doi.org/10.5194/amt-17-4445-2024, 2024.

López-Cayuela, M. Á., Córdoba-Jabonero, C., Bermejo-Pantaleón, D., Sicard, M., Salgueiro, V., Molero, F., Carvajal-Pérez, C. V., Granados-Muñoz, M. J., Comerón, A., Couto, F. T., Barragán, R., Zorzano, M.-P., Bravo-Aranda, J. A., Muñoz-Porcar, C., Costa, M. J., Artíñano, B., Rodríguez-Gómez, A., Bortoli, D., Pujadas, M., Abril-Gago, J., Alados-Arboledas, L., and Guerrero-Rascado, J. L.: Vertical characterization of fine and coarse dust particles during an intense Saharan dust outbreak over the Iberian Peninsula in springtime 2021, Atmos. Chem. Phys., 23, 143–161, https://doi.org/10.5194/acp-23-143-2023, 2023.

López-Cayuela, M.-Á., Herrera, M. E., Córdoba-Jabonero, C., Pérez-Ramírez, D., Carvajal-Pérez, C. V., Dubovik, O., and Guerrero-Rascado, J. L.: Retrieval of Aged Biomass-Burning Aerosol Properties by Using GRASP Code in Synergy with Polarized Micro-Pulse Lidar and Sun/Sky Photometer, Remote Sens., 14, 3619, https://doi.org/10.3390/rs14153619, 2022.

Mereuţă, A., Ajtai, N., Radovici, A. T., Papagiannopoulos, N., Deaconu, L. T., Botezan, C. S., Ştefănie, H. I., Nicolae, D., and Ozunu, A.: A novel method of identifying and analysing oil smoke plumes based on MODIS and CALIPSO satellite data, Atmos. Chem. Phys., 22, 5071–5098, https://doi.org/10.5194/acp-22-5071-2022, 2022.

Milford, C., Torres, C, Vilches, J., Gossman, A. K., Weis, F., Suárez-Molina, D., García, O. E., Prats, N., Barreto, A., García, R. D., Bustos, J. J., Marrero, C. L., Ramos, R., Chinea, N., Boulesteix, T., Taquet, N., Rodríguez, S., López-Darias, J., Sicard, M., Córdoba-Jabonero, C., and Cuevas, E.: Impact of the 2021 La Palma volcanic eruption on air quality: Insights from a multidisciplinary approach, Sci. Total Environ., 869, 161652, https://doi.org/10.1016/j.scitotenv.2023.161652, 2023.

Mortier, A., Goloub, P., Podvin, T., Deroo, C., Chaikovsky, A., Ajtai, N., Blarel, L., Tanre, D., and Derimian, Y.: Detection and characterization of volcanic ash plumes over Lille during the Eyjafjallajökull eruption, Atmos. Chem. Phys., 13, 3705–3720, https://doi.org/10.5194/acp-13-3705-2013, 2013.

Omar, A. H., Winker, D. M., Vaughan, M. A., Hu, Y., Trepte, C. R., Ferrare, R. A., Lee, K.-P., Hostetler, C. A., Kittaka, C., Rogers, R. R., Kuehn, R. E. and Liu, Z.: The CALIPSO Automated Aerosol Classification and Lidar Ratio Selection Algorithm, J. Atmos. Oceanic Technol., 26(10), 1994–2014, https://doi.org/10.1175/2009JTECHA1231.1, 2009.

Ortiz-Amezcua, P., Guerrero-Rascado, J. L., Granados-Muñoz, M. J., Benavent-Oltra, J. A., Böckmann, C., Samaras, S., Stachlewska, I. S., Janicka, Ł, Baars, H., Bohlmann, S., and Alados-Arboledas, L.: Microphysical characterization of long-range transported biomass burning particles from North America at three EARLINET stations, Atmos. Chem. Phys., 17, 5931–5946, https://doi.org/10.5194/acp-17-5931-2017, 2017.

Pappalardo, G., Amodeo, A., Apituley, A., Comeron, A., Freudenthaler, V., Linné, H., Ansmann, A., Bösenberg, J., D'Amico, G., Mattis, I., Mona, L., Wandinger, U., Amiridis, V., Alados-Arboledas, L., Nicolae, D., and Wiegner, M.: EARLINET: towards an advanced sustainable European aerosol lidar network, Atmos. Meas. Tech., 7, 2389–2409, https://doi.org/10.5194/amt-7-2389-2014, 2014.

Papetta, A., Marenco, F., Kezoudi, M., Mamouri, R.-E., Nisantzi, A., Baars, H., Popovici, I. E., Goloub, P., Victori, S., and Sciare, J.: Lidar depolarization characterization using a reference system, Atmos. Meas. Tech., 17, 1721–1738, https://doi.org/10.5194/amt-17-1721-2024, 2024.

Popovici, I. E., Deng, Z., Goloub, P., Xia, X., Chen, H., Blarel, L., Podvin, T., Hao, Y., Chen, H., Torres, B., Victori, S., and Fan, X.: Mobile On-Road Measurements of Aerosol Optical Properties during MOABAI Campaign in the North China Plain, Atmos., 13, 21, https://doi.org/10.3390/atmos13010021, 2022.

Popovici, I. E., Goloub, P., Podvin, T., Blarel, L., Loisil, R., Unga, F., Mortier, A., Deroo, C., Victori, S., Ducos, F., Torres, B., Delegove, C., Choël, M., Pujol-Söhne, N., and Pietras, C.: Description and applications of a mobile system performing on-road aerosol remote sensing and in situ measurements, Atmos. Meas. Tech., 11, 4671–4691, https://doi.org/10.5194/amt-11-4671-2018, 2018.

Qi, S., Huang, Z., Ma, X., Huang, J., Zhou, T., Zhang, S., Dong, Q., Bi, J., and Shi, J.: Classification of atmospheric aerosols and clouds by use of dual-polarization lidar measurements, Opt. Express, 29(15), 23461, https://doi.org/10.1364/OE.430456, 2021.

Riandet, A., Xueref-Remy, I., Popovici, I., Lelandais, L., Armengaud, A., and Goloub, P.: Diurnal and Seasonal Variability in the Atmospheric Boundary-Layer Height in Marseille (France) for Mistral and Sea/Land Breeze Conditions, Remote Sens., 15, 1185, https://doi.org/10.3390/rs15051185, 2023.

Rodríguez, S., Cuevas, E., Prospero, J. M., Alastuey, A., Querol, X., López-Solano, J., García, M. I. and Alonso-Pérez, S.: Modulation of Saharan dust export by the North African dipole, Atmos. Chem. Phys., 15, 7471-7486, https://doi.org/10.5194/acp- 15-7471-2015, 2015.

Rodríguez, S., Alastuey, A., Alonso-Pérez, S., Querol, X., Cuevas, E., Abreu-Afonso, J., Viana, M., Pérez, N., Pandolfi, M., and de la Rosa, J.: Transport of desert dust mixed with North African industrial pollutants in the subtropical Saharan Air Layer, Atmos. Chem. Phys., 11, 6663–6685, https://doi.org/10.5194/acp- 11-6663-2011, 2011.

Sanchez Barrero, M. F., Popovici, I. E., Goloub, P., Victori, S., Hu, Q., Torres, B., Podvin, T., Blarel, L., Dubois, G., Ducos, F., Bourrianne, E., Lapionak, A., Proniewski, L., Holben, B., Giles, D. M., and LaRosa, A.: Enhancing mobile aerosol monitoring with CE376 dual-wavelength depolarization lidar, Atmos. Meas. Tech., 17, 3121–3146, https://doi.org/10.5194/amt-17-3121-2024, 2024.

Schuster, G. L., Dubovik, O., and Holben, B. N.: Angstrom exponent and bimodal aerosol size distributions, J. Geophys. Res.-Atmos., 111, D07207, https://doi.org/10.1029/2005JD006328, 2006.

Sicard, M., Córdoba-Jabonero, C., Barreto, A., Welton, E. J., Gil-Díaz, C., Carvajal-Pérez, C. V., Comerón, A., García, O., García, R., López-Cayuela, M.-Á., Muñoz-Porcar, C., Prats, N., Ramos, R., Rodríguez-Gómez, A., Toledano, C., and Torres, C.: Volcanic Eruption of Cumbre Vieja, La Palma, Spain: A First Insight to the Particulate Matter Injected in the Troposphere. Remote Sens., 14(10), 2470. https://doi.org/10.3390/rs14102470, 2022.

Sinyuk, A., Holben, B. N., Eck, T. F., Giles, D. M., Slutsker, I., Korkin, S., Schafer, J. S., Smirnov, A., Sorokin, M., and Lyapustin, A.: The AERONET Version 3 aerosol retrieval algorithm, associated uncertainties and comparisons to Version 2, Atmos. Meas. Tech., 13(6), 3375-3411, https://doi.org/10.5194/amt-13-3375-2020, 2020.

Smirnov, A., Holben, B. N., Eck, T. F., Dubovik, O., and Slutsker, I.: Cloud-Screening and Quality Control Algorithms for the AERONET Database, Remote Sens. Environ., 73, 337–349, https://doi.org/10.1016/S0034-4257(00)00109-7, 2000.

Shipley, S. T., Tracy, D. H., Eloranta, E. W., Trauger, J. T., Sroga, J. T., Roesler, F. L., and Weinman, J. A.: High spectral resolution lidar to measure optical scattering properties of atmospheric aerosols. 1: Theory and instrumentation, Appl. Opt. 22, 3716-3724, 1983.

Szopa, S., V. Naik, B. Adhikary, P. Artaxo, T. Berntsen, W. D. Collins, S. Fuzzi, L. Gallardo, A. Kiendler-Scharr, Z. Klimont, H. Liao, N. Unger, and P. Zanis, Short-lived Climate Forcers. In Climate Change 2021 – The Physical Science Basis: Working Group I Contribution to the Sixth Assessment Report of the Intergovernmental Panel on Climate Change (1st ed.). Cambridge University Press. https://doi.org/10.1017/9781009157896, 2021.

Tesche, M., Gross, S., Ansmann, A., Müller, D., Althausen, D., Freudenthaler, V. and Esselborn, M.: Profiling of Saharan dust and biomass-burning smoke with multiwavelength polarization Raman lidar at Cape Verde, Tellus B: Chemical and Physical Meteorology, 63 (4), 649-676, https://doi.org/10.1111/j.1600-0889.2011.00548.x, 2011.

Tesche, M., Ansmann, A., Müller, D., Althausen, D., Engelmann, R., Freudenthaler, V. and Groß, S.: Vertically resolved separation of dust and smoke over Cape Verde using multiwavelength Raman and polarization lidars during Saharan Mineral Dust Experiment 2008, J. Geophys. Res., 114, D13202, https://doi.org/10.1029/2009JD011862, 2009b.

Tesche, M., Ansmann, A., Müller, D., Althausen, D., Mattis, I., Heese, B., Freudenthaler, V., Wiegner, M., Esselborn, M., Pisani, G., and Knippertz, P.: Vertical profiling of Saharan dust with Raman lidars and airborne HSRL in southern Morocco during SAMUM, Tellus B , 61(1), 144-164, https://doi.org/10.1111/j.1600-0889.2008.00390.x, 2009a.

Torres, B. and Fuertes, D.: Characterization of aerosol size properties from measurements of spectral optical depth: a global validation of the GRASP-AOD code using long-term AERONET data, Atmos. Meas. Tech., 14, 4471–4506, https://doi.org/10.5194/amt-14-4471-2021, 2021.

Torres, B., Dubovik, O., Fuertes, D., Schuster, G., Cachorro, V. E., Lapyonok, T., Goloub, P., Blarel, L., Barreto, A., Mallet, M., Toledano, C., and Tanré, D.: Advanced characterisation of aerosol size properties from measurements of spectral optical depth using the GRASP algorithm, Atmos. Meas. Tech., 10, 3743–3781, https://doi.org/10.5194/amt-10-3743-2017, 2017.

Tsekeri, A., Lopatin, A., Amiridis, V., Marinou, E., Igloffstein, J., Siomos, N., Solomos, S., Kokkalis, P., Engelmann, R., Baars, H., Gratsea, M., Raptis, P. I., Binietoglou, I., Mihalopoulos, N., Kalivitis, N., Kouvarakis, G., Bartsotas, N., Kallos, G., Basart, S., Schuettemeyer, D., Wandinger, U., Ansmann, A., Chaikovsky, A. P., and Dubovik, O.: GARRLiC and LIRIC: strengths and limitations for the characterization of dust and marine particles along with their mixtures, Atmos. Meas. Tech., 10, 4995–5016, https://doi.org/10.5194/amt-10-4995-2017, 2017.

Wang, D., Stachlewska, I. S., Delanoë, J., Ene, D., Song, X., and Schüttemeyer, D.: Spatio-temporal discrimination of molecular, aerosol and cloud scattering and polarization using a combination of a Raman lidar, Doppler cloud radar and microwave radiometer, Opt. Express, 28, 20117, https://doi.org/10.1364/OE.393625, 2020.

Weitkamp, C. (Ed.): Lidar: range-resolved optical remote sensing of the atmosphere, Springer, New York, 455 pp., 2005.

Welton, E. J., Stewart, S. A., Lewis, J. R., Belcher, L. R., Campbell, J. R., and Lolli, S.: Status of the Micro Pulse Lidar Network (MPLNET): Overview of the network and future plans, new version 3 data products, and the polarized MPL, EPJ Web Conf., 176, 09003, https://doi.org/10.1051/epjconf/201817609003, 2018.

Welton, E. J. and Campbell, J. R.: Micropulse Lidar Signals: Uncertainty Analysis. J. Atmos. Oceanic Technol., 19 (12), 2089-2094, https://doi.org/10.1175/1520-0426(2002)019<2089:MLSUA>2.0.CO, 2, 2002.

Welton, E. J., Campbell, J. R., Spinhirne, J. D., and Scott Iii, V. S.: Global monitoring of clouds and aerosols using a network of micropulse lidar systems, Second International Asia-Pacific Symposium on Remote Sensing of the Atmosphere, Environment, and Space, Sendai, Japan, 151, https://doi.org/10.1117/12.417040, 2001.